Progress in Additive Manufacturing (2025) 10:5093–5115
https://doi.org/10.1007/s40964-024-00891-8

FULL RESEARCH ARTICLE

Phase-field modeling of the morphological and thermal evolution of additively manufactured polylactic acid layers and their influence on the effective elastic mechanical properties

Ahmed Elmoghazy[1,2] · Anselm Heuer[4] · Aron Kneer[1,5] · Martin Reder[1,2] · Andreas Prahs[1] · Daniel Schneider[1,2,3] · Wilfried V. Liebig[4] · Britta Nestler[1,2,3]

Received: 8 August 2024 / Accepted: 22 November 2024 / Published online: 18 December 2024

Abstract

This study presents a comprehensive simulation of the fused deposition modeling (FFF) process of polylactic acid (PLA) using the multiphase-field method. Compared to existing works, this work aims to simulate the overall FFF process. It combines temperature evolution, viscous flow, polymer crystallization, and residual strain calculations within the microstructure with mechanical property analysis in a single study. Simulation studies were done in the case of the single layer to study the flowing effect of the filament and the distribution of temperature, viscosity, and relative crystallinity throughout the cooling process. Afterward, a system of layers with three rows and three columns was investigated. The nozzle temperature, bed temperature, viscosity, and layer height were varied, and for each case the porosity was calculated. After running mechanical loading simulations on each case, the effective Young's modulus was calculated. The simulations show that increasing the nozzle and bed temperatures leads to a decrease in the porosity, while increasing the layer height increases the distortion in the pores' shapes without significantly affecting the porosity. The decrease in porosity leads to an increase in the effective Young's modulus of the structure in a linear trend within the investigated porosities. The Young's modulus–porosity relation was validated with experimental values from the literature within an average error of 3.6 %.

Keywords Additive manufacturing · kadi4mat · Flow dynamics · Polymer crystallization · Effective material properties · Fused filament fabrication

✉ Ahmed Elmoghazy
ahmed.elmoghazy@kit.edu

Anselm Heuer
anselm.heuer@kit.edu

Aron Kneer
a.kneer@tinnit.de

Martin Reder
martin_dominik.reder@h-ka.de

Andreas Prahs
andreas.prahs@kit.edu

Daniel Schneider
daniel.schneider@kit.edu

Wilfried V. Liebig
wilfried.liebig@kit.edu

Britta Nestler
britta.nestler@kit.edu

[1] Institute for Applied Materials - Microstructure Modelling and Simulation (IAM-MMS), Karlsruhe Institute of Technology (KIT), Straße am Forum 7, 76131 Karlsruhe, Germany

[2] Institute of Digital Materials Science (IDM), Karlsruhe University of Applied Sciences, Moltkestraße 30, 76133 Karlsruhe, Germany

[3] Institute of Nanotechnology (INT), Karlsruhe Institute of Technology (KIT), Hermann-von-Helmholtz-Platz 1, Eggenstein-Leopoldshafen, 76344 Karlsruhe, Germany

[4] Institute for Applied Materials - Materials Science and Engineering (IAM-WK), Karlsruhe Institute of Technology (KIT), Kaiserstrasse 12, 76131 Karlsruhe, Germany

[5] TinniT Technologies GmbH, Essenweinstrasse 25, 76131 Karlsruhe, Germany

1 Introduction

Motivation: The concept of three-dimensional (3D) printing, also known as additive manufacturing, has marked a paradigm shift in the way we conceive, design, and produce objects. The technology originated in the 1980s with the pioneering work of Charles Hull, who introduced the world to stereolithography [1]. This early approach to 3D printing involved the use of UV lasers to solidify photopolymer to create solid, 3D objects layer by layer. Over the following decades, 3D printing technologies diversified and improved significantly. Among the various techniques that emerged, fused filament fabrication (FFF), patented by Scott Crump in the late 1980s [2] became particularly prominent due to its accessibility and versatility. The process starts with a digital design of an object, often created using computer-aided design (CAD) software, which is then converted into a format that a 3D printer can interpret. FFF technology works by extruding a thermoplastic filament, which is heated above its melting point and then selectively deposited layer by layer following the 3D model's path. After deposition, the material solidifies quickly to form a solid structure. This procedure is repeated layer upon layer until the complete 3D object is formed. The material, layer thickness, resolution, orientation, and fill density are among the parameters that can be controlled in this process, making FFF versatile in its application. This technology's ascendancy has enabled widespread use in industries ranging from automotive to aerospace, medical, and consumer goods. It has revolutionized prototyping, given birth to the concept of rapid manufacturing and customized production. Indeed, the evolution of 3D printing, and in particular FFF, from a niche technology to a mainstream manufacturing process, marks a significant milestone in the ongoing quest for innovation and efficiency in product design and development. In recent years, significant progress has been made in the design and analysis of 3D printed PLA-based structures with tailored mechanical and functional properties. PLA, being a biodegradable and biocompatible polymer, has gained attention in various applications due to its environmental friendliness and ease of processing in additive manufacturing techniques such as FFF. For instance, adding natural fibers, such as flax, has been shown to significantly enhance the tensile and flexural strength of PLA-based structures. The careful control of factors such as fiber orientation, infill density and surface treatments during the printing process allows for further tuning of the material's properties, enabling the production of components with targeted mechanical characteristics [3]. Recent research has explored the concept of functionally graded materials (FGMs) in 3D printing, where the material's properties are varied spatially to meet specific design and functional requirements. This allows for the creation of PLA-based structures with tailored properties—stronger in one region while more flexible in others—suitable for complex, multifunctional applications [4]. These advancements underline the importance of the material–process–property relationship in additive manufacturing, where the integration of process optimization, material selection, and advanced modeling techniques can significantly impact the effective mechanical and functional properties of the final structure.

Process-induced heterogeneity: Fused filament fabrication, despite its widespread application, harbors inherent challenges that may influence the quality of the final product. The thermal nature of the FFF process can introduce heterogeneities at the micro and mesoscale, prominently in the form of pores. These defects vary in size, shape, and distribution. Their occurrence in the material heavily depends on the precise process parameters employed during fabrication [5]. The presence of these pores can significantly impact the internal structure of the deposited materials. They can act as stress concentrators, negatively affecting the mechanical properties of the final product. This includes aspects such as tensile strength, stiffness, and durability, often leading to anisotropy and reduced overall part performance [6, 7]. The fabrication process parameters in FFF play a crucial role in the formation of pores within the 3D printed structure. These parameters include extrusion temperature, print speed, layer thickness, and infill density, among others, and each can significantly influence the microstructure and thus the mechanical properties of the final product.

Effect of process parameters on the effective mechanical properties : There exists a number of studies to investigate the effect of several process parameters on the resulting microstructure as well as the mechanical properties of the print [8–12]. Thereby, experimental or numerical approaches are employed. Taking a look into the experimental works, in Khetwani et al. [13], it was observed that an increase in the bed temperature leads to an increase in the tensile and flexural strength of the build, while an increase in the layer thickness led to a decrease in the tensile strength and an increase in the flexural strength. That finding was confirmed by Holm [14] as a part of his investigation into the effect of layer height on ultimate tensile strength and tensile modulus. Apart from the layer thickness, the printing speed also contributes to the mechanical properties of the final build. Ning et al. [15] and Christiyan et al. [16] show that higher printing speed reduces the printing time and thus the production costs. However, the tensile strength was reduced. Another parameter to be considered is the infill percentage. This parameter is significant in saving material, lower production costs, and reducing the weight of the part. The infill percentage also affects the elastic modulus of the part as

shown in a comprehensive study by Alafaghani et al. [17]. Therein, the infill percentage was shown to increase the tensile strength, yield strength, and elastic modulus. This is mainly due to the density of pores in the part, which are themselves non-load-bearing. In that same study, the effect of extrusion temperature was also investigated. It was observed that an increase in extrusion temperature was linked to improved mechanical properties up to a certain limit. This can be explained by the better fusion between the layers, which contributes to its load-bearing ability.

Recent approaches to model the FFF process: The work done by Descher [18] focuses on crystallization processes in polymer melts. He integrates a novel crystallization model derived from dynamic scanning calorimetry data, which provides an accurate prediction of crystallinity across different cooling rates. This model's success depends on the thermorheological generalized Maxwell model for melt flow behavior and its implementation in the OpenFOAM CFD library, presenting a robust framework for predicting the interactions between the melt and solidified domains within the polymer. In the study by Lee et al. [19], the researchers investigate the impact of temperature history on the crystalline morphology of polyetheretherketone (PEEK) during the FFF process. They employ differential scanning calorimetry (DSC) and polarized optical microscopy to assess the effects of cooling rates on the material's degree of crystallinity, finding that slower printing speeds and higher nozzle temperatures lead to enhanced mechanical properties due to increased degree of crystallinity. Finite element (FE) simulations using the commercial software ABAQUS further validate the experimental findings, solidifying the assertion that temperature is a linchpin in determining the mechanical integrity of 3D printed parts. Lei et al. [20] offer a different perspective by investigating the PLA/GNPs nanocomposite material. Their research underscores the significance of nozzle temperature and printing speed, showing that these parameters substantially influence the cross-sectional morphology of the printed filaments. The study combines numerical models that account for the non-Newtonian fluid behavior with experimental trials to measure tensile strength as a function of the said process parameters. Lepoivre et al. [21] focuses on heat transfer and adhesion phenomena in FFF. By utilizing infrared cameras and pyrometers to capture temperature profiles and employing COMSOL Multiphysics for numerical simulations, they provide critical insights into the thermal behavior of polymers like its thermal history and degree of adhesion. Tichý et al. [22] contribute to the field by developing FE models to study the temperature distribution in different parts of the FFF printer during operation. Their approach highlights the printer's components' role in the overall printing process and gives crucial information about the cooling rates as well as the thermal history and distribution inside the printer and along the strand.

Recent fluid flow simulations of the melt: The work of Mishra et al. [23] shifts the focus to the challenge of simulating melt flow dynamics within the nozzle. By implementing the Cross–Williams–Landel–Ferry (Cross-WLF) viscosity and pressure–volume–temperature (PVT) density models into ANSYS Fluent simulations, they show the complex interaction of viscosity, temperature, and velocity in acrylonitrile butadiene styrene (ABS) and PLA during FFF. Their work clearly shows the importance of properly modeling the rheological properties of the material, since the corresponding model significantly affects the morphology of the strand. Similar results were found by the work of Seta et al. [24] which presents a three-dimensional model to simulate the shape morphology. Therein, OpenFOAM simulations are carried out demonstrating how printing conditions influence morphology of the resulting strands as well. Zhou et al. [25] round out the research by examining the bond formation between strands in both PEEK and PLA materials. Their comprehensive approach, which includes both simulation and experimental validation, shows how the process parameters such as gap distance and printing speed influence the degree of bonding and porosity, affecting the mechanical properties of the final product such as the tensile strength of the print. It was qualitatively shown that increase in porosity and decrease in bonding degree lead to decrease in tensile strength.

Objective of the current work: In the current work, a workflow was implemented in the open-source software, Kadi4Mat [26], to simulate the FFF process using the inhouse simulation software PACE3D (Parallel Algorithms for Crystal Evolution in 3D) [27]. The FFF process was modeled to investigate the impact of various parameters on the microstructural evolution of the printed layers. Specifically, parameters such as nozzle temperature, bed temperature, the geometry of the layer, and the filament type were taken into account. Through the implementation of this model, it was possible to simulate and study the formation and evolution of pores within the printed layers, their shape, and their size. Following the study of temperature, crystallinity, and morphological evolution, the effect of these pores on the mechanical properties was assessed. Specifically, the impact on the effective Young's modulus was evaluated. The effective Young's modulus is a crucial mechanical property as it defines the stiffness of a material under deformation, thus playing a pivotal role in determining the material's overall performance and suitability for various applications. It has been assumed that the material deforms in a purely elastic manner. This allows to straightforwardly determine the effect of the pores on the effective elastic properties. The implementation of this workflow and the subsequent findings provide a deeper understanding of the inherent relationship between the process parameters, morphological evolution, and mechanical properties in the FFF process. Furthermore,

it highlights the potential for using advanced modeling techniques to enhance the predictability and optimization of 3D printing technologies.

Originality: The literature emphasizes the importance of capturing the complex interplay of processes that occur during FFF. Compared to existing works, this work aims to simulate the overall FFF process. It combines temperature evolution, viscous flow, and polymer crystallization within the microstructure with mechanical property analysis in a single study. In addition, the printing of multiple layers is considered, which raises the possibility of studying the interaction between two layers of the filament.

Outline: In Sect. 2, the overall workflow among the contributing partners is presented. The material characterization of PLA is described in Sect. 3. Section 4 presents the considered numerical models used in the simulation studies. The simulation procedure as well as the simulation studies and their results are discussed in Sect. 5. The concluding remarks are given in Sect. 6.

2 Overview of the workflow

The general workflow is presented in Fig. 1, where the whole process is depicted from start to finish. Experimental studies and material characterization processes are displayed by yellow boxes, analytical analysis on the viscosity data, as well as simulation studies on the flow behavior of a single strand using different process parameters are shown in teal. Finally, analysis of

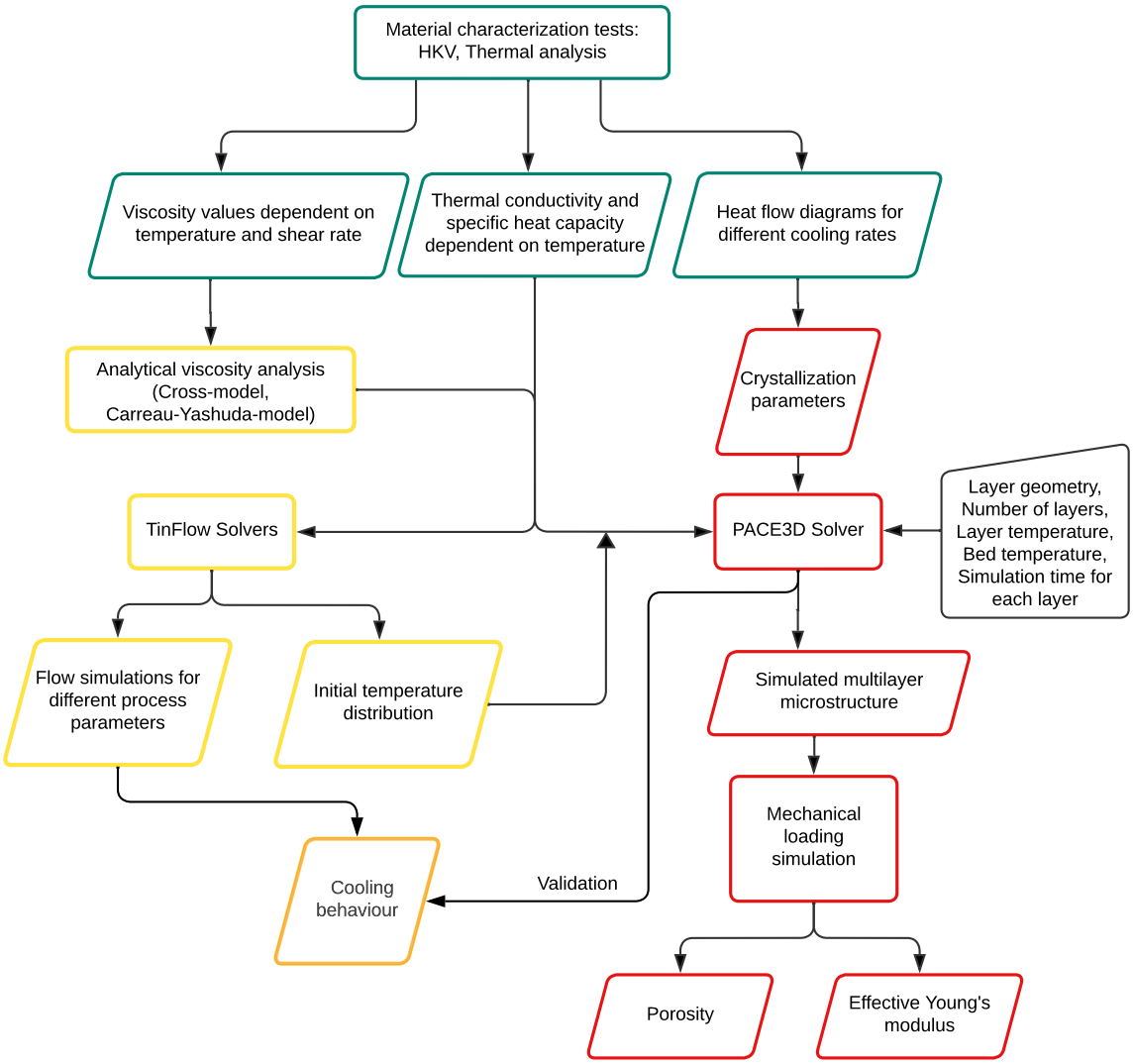

Fig. 1 Overview of the workflow between the working partners. The part outlined in teal represents material characterization steps, red represents the working steps related to microstructure simulation and microstructure–property characterization, while yellow represents the processes-related numerical viscosity, single strand flow simulations, as well as validation for the temperature solver

the crystallization parameters, running simulation studies using PACE3D, as well as the post-processing of the results to calculate the porosity and the effective Young's modulus contribute to the workflow by the red boxes. After procuring the material (PLA filament), material characterization tests are done to identify the important material parameters. Rheological tests yield experimental values for the shear viscosity dependent on the temperature and shear rate. DSC measurements were done to determine the specific heat capacity as well as cooling rate-dependent heat flow for crystallinity analysis. The rheological results were analyzed analytically using the Cross-WLF model and the Carreau–Yashuda model. The model that delivered the most accurate fit was used in the subsequent steps, as will be shown in Sect. 5. This information flows directly into the TinFlow solvers developed by TinniT Technologies GmbH to run flow simulations for different process parameters, taking into consideration the flow inside the nozzle as well as the temperature, concentration, and viscosity distribution of a deposited filament. These investigations have been published in [28]. The output of the analytical viscosity analysis, thermal properties from the experimental work, crystallization parameters, as well as the initial temperature distribution flow into the PACE3D solver. Further manual inputs include the individual layer geometry, number of layers to be simulated, layer temperature (nozzle temperature), bed temperature, and simulation time for each layer. The resulting structures are evaluated with regard to their porosity and additional mechanical simulations are conducted to determine their effective Young's modulus. This part of the workflow is explained in more details in Sect. 5 as well as the simulation results.

3 Material characterization tests

3.1 Determination of shear viscosity

The shear viscosity was determined using two different methods depending on the shear rate. Within the shear rates 1/s and 400/s, the shear viscosity was measured for different temperatures using a rotary rheometer MCR 501 from Anton Paar. The measurement geometry plate–plate and an oscillating mode were used. Between the shear rates 200/s and 1000/s, the shear viscosity for different temperatures was measured with the high pressure capillary rheometer (HCR) Rheograph 20 from Göttfert Werkstoff-Prüfmaschinen GmbH. A capillary with a length of 30 mm and a diameter of 1 mm was used. The measuring range of the pressure sensor used is up to 1000 bar, whereby 1% of the maximum pressure can still be reliably resolved. The plastic was first heated in the HCR, then compressed and then a volume flow was established at a shear rate lower than the shear rate to be measured. This was followed by the measurement itself. Owing to to inlet pressure losses, only an apparent shear viscosity can be measured with the HCR, which is why a correction was carried out with the help of the measured values from the rotational rheometer. The shear rates 200/s and 400/s were determined in an overlapping manner so that the measured values from the HCR could be matched to those from the rotational rheometer. Previous measurements with different capillaries have shown that such a procedure provides a valid correction. Figure 2 shows the results achieved from the viscosity measurement for PLA. The dynamic viscosity drops drastically as the shearing rate increases and has the highest values at very low shearing rates. The temperature dependency is just as important as it can be seen from the figure.

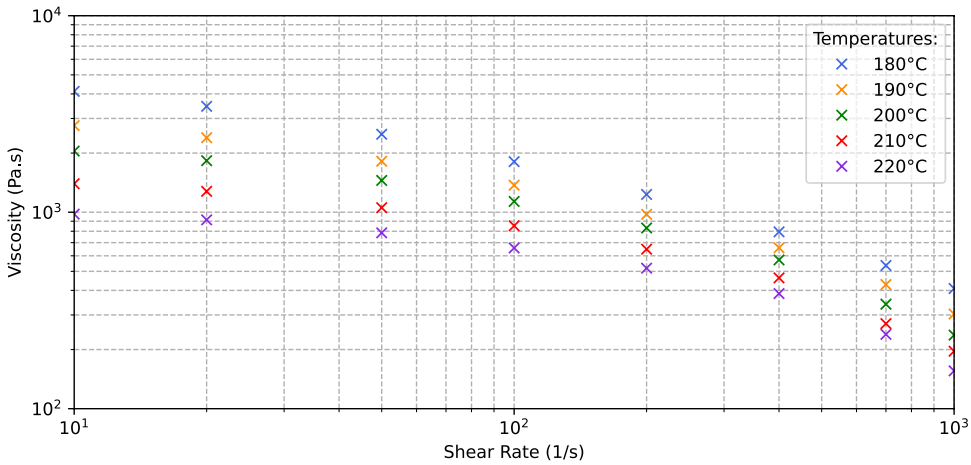

Fig. 2 Measured dynamic viscosity for the material PLA

3.2 Thermal analysis by differential scanning calorimetry

To determine the amount of heat emitted or absorbed during a constant temperature change, DSC measurement was carried out with the DSC 1 Star system from METTLER TOLEDO in a temperature range from 25°C to 210°C. A measurement cycle consisted of heating with 5°C/min, variable cooling, and further heating with 5°C/min. The cooling rates 2°C/min, 4°C/min, 8°C/min, 14°C/min, and 20°C/min were investigated. Each measurement was repeated with a second specimen for statistical validation. An aluminum crucible was used to take a specimen and it was flushed with nitrogen during the measurement.

To calculate the degree of crystallinity, a specific enthalpy of fusion ΔH_0 of 93 J/g was assumed for 100 % pure crystals of PLA. The crystallinity $X_{abs.}$ after cooling the specimen with a specific cooling rate was calculated according to the equation

$$X_{abs.} = \frac{\Delta H_{Fus} - \Delta H_{ColdC}}{\Delta H_0} \cdot 100, \quad (1)$$

where ΔH_{Fus} corresponds to the enthalpy of fusion after the second heating and ΔH_{ColdC} to the enthalpy released during cold crystallization. The crystallinity was determined by averaging the two separate measurements, where the difference between them was very small.

The cooling curves in Fig. 3 show the thermal behavior of PLA as it is cooled at different rates, as measured by DSC. The rates range from 2°C/min to 20°C/min, each represented by a distinct color. A key observation is that the peak shapes vary with cooling rate. At lower cooling rates (2°C/min and 4°C/min), the crystallization peaks are more pronounced and occur at higher temperatures indicating higher degrees of crystallinity. This is explained as follows: lower cooling allows PLA chains more time to organize into a crystalline structure. As the cooling rate increases, the peaks become broader and shift to lower temperatures, with the 20°C/min curve showing a much less distinct peak. This shift is indicative of less organized, more rapid crystallization, and even suppressed crystallization can be extrapolated if the cooling rate is to be slightly higher.

The crystallinity properties of PLA are shown in Table 1 as determined by DSC measurements for various cooling rates, where T_c is the crystallization temperature, T_g is the glass transition temperature, ΔH_c is the crystallization enthalpy, and X_{abs} is the absolute degree of crystallinity. It is apparent that crystallization temperature decreases with increasing cooling rates. This is typical since at higher cooling rates, there is less time for the PLA molecules to arrange into a well-ordered crystalline structure, causing crystallization to occur at a lower temperature. The glass transition temperature remains relatively stable at around 58.5°C, except for the highest cooling rate of 20°C/min where a jump to 62.7°C can be seen. This is probably due to a test artifact as the test done at this cooling rate was made at

Table 1 Crystallinity properties for PLA for different cooling rates

Cooling rate (°C/min)	T_c(°C)	T_g(°C)	ΔH_c (J/g)	$X_{abs.}$ (%)
2	119.8	58.3	28.2	36.0
4	112.5	59.7	25.0	31.0
8	101.6	58.3	14.0	21.0
14	101.8	58.1	3.0	7.0
20	100.2	62.7	1.3	1.8

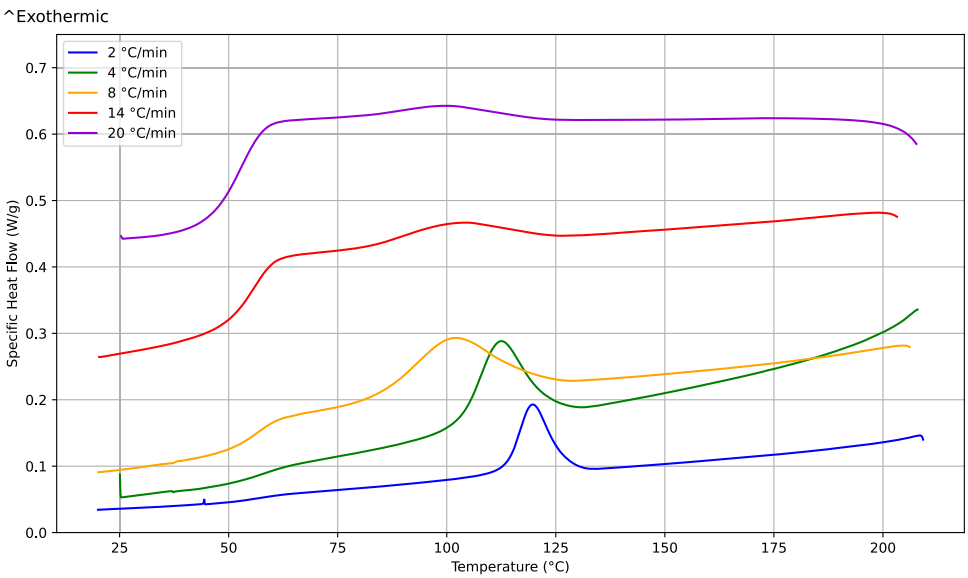

Fig. 3 Cooling curves for PLA from DSC measurements for different cooling rates

a much earlier date than the others. The enthalpy ΔH_c of crystallization, which is a measure of the heat released due to crystallization, and the degree of crystallinity $X_{abs.}$ both decrease with increasing cooling rate. At a slower cooling rate (2°C/min), the material has a higher enthalpy of crystallization and degree of crystallinity, indicating a greater extent of crystalline structure formation. Conversely, at the fastest cooling rate (20°C/min), the values are much lower, suggesting minimal crystalline structure. These observations are consistent with the DSC cooling curves provided earlier, where slower cooling rates showed more pronounced exothermic peaks, indicative of a higher degree of crystallization. The broader and lower-temperature peaks at higher cooling rates correspond to the lower ΔH_c and $X_{abs.}$ values in the table, reflecting the reduced time for crystals to form.

3.3 Determination of specific heat capacity

Depending on the temperature of the polymer, the specific heat capacity was determined using a temperature-modulated DSC (TMDSC) measurement. In principle, this measurement method operates in such a way that small temperature changes with alternating signs and fixed amplitude and frequency are applied to the underlying heating rate. However, it is only possible to calculate the dynamic specific heat capacity from the resulting heat flow signal of the measurement. A newer measurement method called TOPEM from METTLER TOLEDO was therefore used to determine the quasi-static specific heat capacity. Here, stochastic temperature changes with fixed amplitude, but random duration are used. The measurement was carried out with the DSC 1 Star system from METTLER TOLEDO in a temperature range from 30 to 220 °C. The underlying heating rate was 1K/min and the fixed amplitude was ± 0.5K/min. The switching time range, which limits the random duration of the temperature changes, was in the range of 15–30 s. For statistical validation, the measurement was taken on two different specimens and the average was calculated. An aluminum crucible was used to take a specimen and it was flushed with nitrogen during the measurement.

The experimentally determined specific heat capacity of PLA is shown in Fig. 4. The values are taken as an average between two different measurements. Sharp changes in the heat capacity are seen at the melting temperature at 145 to 3.00 J/(Kg °C) and at the glass transition temperature range ending at around 50 °C to almost 1.10 J/(Kg °C) in the glassy state, while the base line is around 1.75 J/(Kg °C).

4 Numerical models

Illustration of the simulation procedure: The objective of this study is to simulate the FFF process over the entire temperature range. To this end, temperature evolution, viscous flow and polymer crystallization within the microstructure, and mechanical property analysis are addressed in a single study. Within the temperature range between nozzle temperature and bed temperature, the viscous flow of the filament is modeled by means of the Navier–Stokes equation combined with the equation of heat evolution. The crystallization within the layer is modeled by the Nakamura crystallization model coupled with the equation of heat conduction. Below the bed temperature, the effective elastic properties are obtained by load simulations that account for solid mechanics. In this regard, the shrinkage due to the crystallization process is taken into account as eigenstrain. Moreover, small strains as well as small strain rates are considered, and no phase evolution is present. Thus, a coupling between solid mechanics and the temperature evolution is neglected [29]. In all simulations, i.e., fluid flow, crystallization, determination of effective mechanical properties, the multiphase-field method [30] is employed for the diffuse

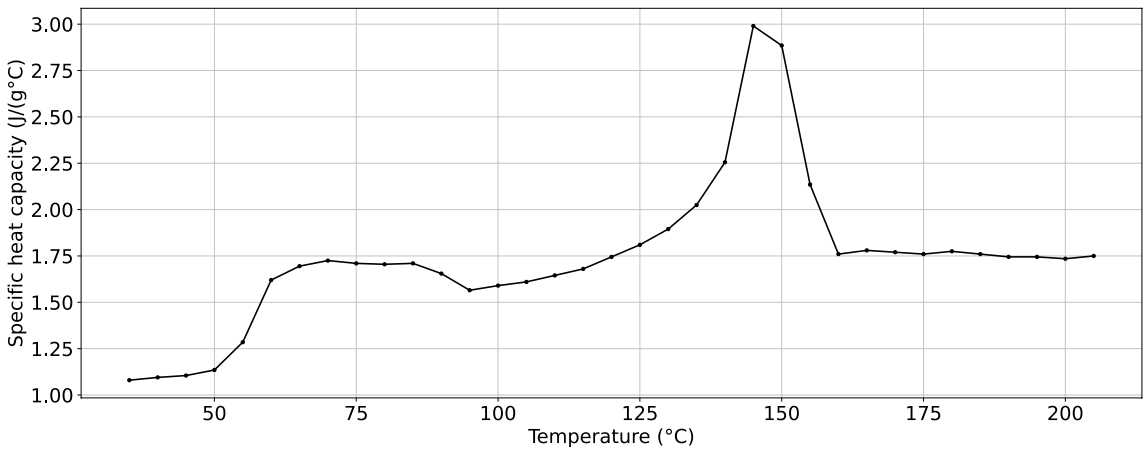

Fig. 4 Specific heat capacity for PLA as function of temperature

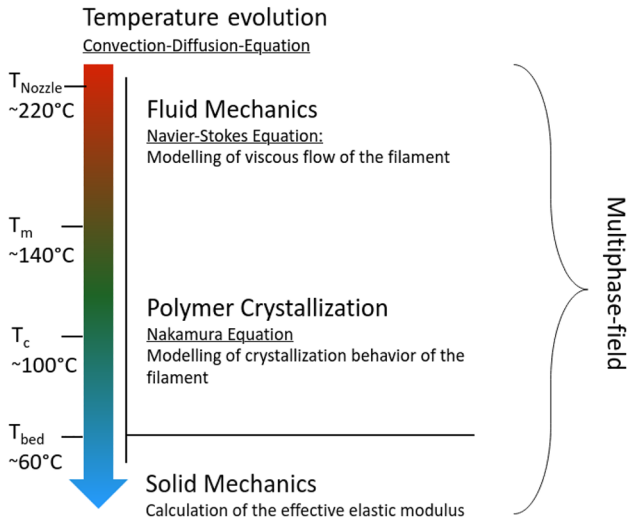

Fig. 5 Overview of the numerical models solved within the temperature range of the FFF process

parametrization of the interfaces. The interplay between the different temperature domains and the considered models is illustrated in Fig. 5.

4.1 Phase-field method

Considered contributions to the free energy

The subsequent models are based on the phase-field method, which is employed for geometry parameterization of different physically distinguishable regions such as different fluid or solid phases occurring in the computational domain. The phase-field model is characterized by introducing a phase variable (or an order parameter) $\phi_\alpha \in [0,1]$ for each phase, which can be understood as local volume fraction of the phase α in space and time. This results in the phase-field tuple $\boldsymbol{\phi} = \{\phi_1, \dots, \phi_N\}$, where N denotes the number of phases considered. Within the phase-field method, the interface between two phases is modeled by a diffuse interface with a smooth transition of the order parameter from 0 to 1. Since the order parameters are interpreted as the volume fractions of the corresponding subregions, they are subjected to the summation constraint $\sum_{\alpha=1}^{N} \phi_\alpha(\boldsymbol{x}, t) = 1$. In this work, two phases are considered where ϕ_1 represents the PLA phase and ϕ_2 is the air phase.

The starting point of the phase-field model is the free energy functional of the system, which is the sum of the interfacial free energy density contribution (including the gradient term and the potential term) as well as the bulk contribution. This is shown in the following equation system:

$$\mathcal{F} = \mathcal{F}_{\text{interface}} + \mathcal{F}_{\text{bulk}} \tag{2a}$$

$$= \int_V f_{\text{gradient}}(\boldsymbol{\phi}, \nabla\boldsymbol{\phi}) + f_{\text{potential}}(\boldsymbol{\phi}) + f_{\text{bulk}}(\boldsymbol{\phi})\, \mathrm{d}V. \tag{2b}$$

On the one hand, in the context of fluid flow, vanishing bulk contributions in the free energy functional are considered [31, 32]. On the other hand, in the context of solid mechanics, the evolution of strains contribute to the free energy of the system. However, since no phase transformation due to mechanical driving forces is considered, the bulk free energy is taken to be zero. The interplay between the gradient and the potential term leads to having a stable interface between the phases. There exist many formulations for both terms and how they should be combined. An overview on that topic can be found in Daubner et al [33]. Following Nestler et al. [30], the gradient contribution for a two-phase system (where $\phi_2 = 1 - \phi_1$) is given as

$$f_{\text{gradient}}(\boldsymbol{\phi}, \nabla\boldsymbol{\phi}) = \epsilon\gamma_{12}\left(\nabla\phi_1\right)^2, \tag{3}$$

where $\gamma_{\alpha\beta}$ is the interfacial energy density between two phases, and ϵ a parameter determining the width of the diffuse interface and $\left(\nabla\phi_1\right)$ is the spatial variation of the order parameter ϕ_1. Forr the potential term, the multi-obstacle potential is used in this form

$$f_{\text{potential}}(\boldsymbol{\phi}) = \frac{16\gamma_{12}}{\epsilon\pi^2} \cdot \phi_1(1-\phi_1). \tag{4}$$

The usage of this potential leads to the equilibrium interface width $\pi^2\epsilon/4$.

Evolution equation of the order parameter: Employing the multiphase-field formulation from Nestler et al. [30] yields the system of Allen–Cahn equations for the temporal and spacial evolution of the phases in the system:

$$\dot{\phi}_\alpha = -M\frac{\delta\mathcal{F}}{\delta\phi_\alpha} - \lambda, \tag{5}$$

where M is the mobility, λ is a Lagrange multiplier ensuring the summation constraint ($\sum_{\alpha=1}^{N} \phi_\alpha(\boldsymbol{x}, t) = 1$) is fulfilled [30], and the operator $\delta(\cdot)$ denotes a variation. Here, $\dot{\phi}_\alpha$ is the material time derivative of the order parameters and is equal to $\partial_t\phi_\alpha + \mathbf{u} \cdot \nabla\phi_\alpha$. Under thermodynamics equilibrium and with vanishing mobilities (approaching the sharp interface assumption), the evolution equation is reduced to the convective transport equation. The evolution equation in the form of Eq. (5) is used in conjunction with the fluid flow model (described later in Sect. 4.3) from where the velocity vector $\mathbf{u}$ is calculated. Later in Sect. 4.5, as the small deformations solid mechanics model is introduced, no evolution takes place as the velocity becomes zero. In this case, the phase field is used namely to distinguish between different phases with different mechanical properties.

4.2 Heat transport model

Equation of heat conduction: The correct modeling of the cooling of the filament is of great importance, since all other physical processes depend on the temperature values inside the domain, e.g., viscosity, thermal capacity, crystallization parameters, and Young's modulus. The convection–diffusion heat transport equation is considered, which is written as

$$\frac{\partial \theta}{\partial t} = \underbrace{\frac{1}{\rho c_v}\nabla \cdot (\kappa \nabla \theta)}_{\text{Diffusion term}} - \underbrace{\mathbf{u} \cdot \nabla(\theta)}_{\text{Convection term}} + \underbrace{R}_{\text{Source term}}, \tag{6}$$

where $\partial\theta/\partial t$ represents the temperature evolution, κ the thermal conductivity of the material, ρ the density, and c_v the specific heat capacity. In the convective term side, $\mathbf{u}$ is used to denote the velocity vector which is calculated in the Navier–Stokes equation (as shown in Sect. 4.3). The convective term is necessary to be able to correctly predict the cooling behavior due to the movement of air and the flow of the filament simultaneously. The source term R consists of only one contribution, which is the exothermic release of heat due to the crystallization process of the polymer and leads to an increase in the temperature of the system. This term will be discussed later in Sect. 4.4.

Phase-dependent parameters: The thermal diffusivity in Eq. (6) is phase dependent in this context. Therefore, a linear interpolation is applied to retrieve the value of this quantity along the interface. The interpolation then reads

$$\kappa = \sum_{\alpha=1}^{N} \phi_\alpha \kappa_\alpha, \quad \rho c_v = \sum_{\alpha=1}^{N} \phi_\alpha \rho_\alpha c_{v,\alpha}. \tag{7}$$

Typically quantities like the density, thermal conductivity, and specific heat capacity are be temperature dependent. However, due to lack of data, the thermal conductivity and density are assumed to be constant with temperature. This assumption is justified due to the low variation of both parameters along the temperature scale.

4.3 Fluid flow model

Two-phase flow: For the fluid flow model, the phase-field method is coupled with the two-phase flow model known as the Hohenberg–Halperin type model on the basis of the Navier–Stokes equation. The Navier–Stokes equation system is known in this form:

$$\rho\left(\frac{\partial \mathbf{u}}{\partial t} + \mathbf{u} \cdot \nabla \mathbf{u}\right) = -\nabla p + \nabla \cdot \left(\mu\left(\nabla \mathbf{u} + (\nabla \mathbf{u})^T\right)\right) + \rho \mathbf{f}_\mathbf{v} + \mathbf{K}, \tag{8a}$$

$$\nabla \cdot \mathbf{u} = 0. \tag{8b}$$

The equation system showed above contains the momentum equation (8a) as well as the continuity equation (8b) for incompressible flow. In equation (8a), $\mathbf{u}$ is the velocity vector, ρ the density, p the pressure, μ the dynamic viscosity, and $\mathbf{f}_v$ the body force (for example: gravity). $\mathbf{K}$ is the capillary term arising in the fluid–fluid interface due to the surface tension effect. The density and the dynamic viscosity values inside the diffuse interface region of the two phases are calculated through a linear interpolation of the values in the separate phases using

$$\rho = \sum_{\alpha=1}^{N} \phi_\alpha \rho_\alpha, \quad \mu(\theta) = \sum_{\alpha=1}^{N} \phi_\alpha \mu_\alpha(\theta). \tag{9}$$

Since one is dealing with multiphase flow, the additional capillary term $\mathbf{K}$ is to be considered in the Navier–Stokes equation. The capillary term derived from Jacqmin [31] and Kim et al. [34] for two-phase fluid flow is taken in its potential form and reads

$$\mathbf{K} = -\nabla \cdot \mathbf{\Theta} = -2A(\gamma_{12})\nabla \cdot [(\nabla \phi_1 \otimes \nabla \phi_1)], \tag{10}$$

where $\mathbf{\Theta}$ is the capillary tensor, γ_{12} is the surface tension of the fluid interface between both phases, and A is a constant related to the potential term, cf. [35]. Due to the lack of data on the variation of the surface tension of PLA along the temperature axis, the surface tension is assumed to be constant.

The Hohenberg–Halperin model [36] is introduced in the Navier–Stokes equation system by including an evolution equation of one of the fluid phases and calculating the other phase using the summation constraint $\phi_1^{fluid} + \phi_2^{fluid} = 1$. The evolution equation can take the form of a Cahn–Hilliard or a volume preserving Allen–Cahn type equation. The model has been introduced, described, and validated in greater detail in Reder et al. [35]. In the present work, the volume preserving Allen–Cahn approach is used, whereby equation 5 is augmented with an additional Lagrange multiplier ensuring volume preservation of all phases [37].

Analytical analysis of viscosity measurements : Plastics such as PLA exhibit non-Newtonian viscous behavior and can be modeled as a generalized Newtonian fluid. This means that the dynamic viscosity of the polymer not only has a temperature dependency, but also a shear rate dependency. Specifically, liquid plastic exhibits a low viscosity at high shear rates and a high viscosity at low shear rates. This is particularly important in connection with the printing process. The filament is mechanically fed through the extruder to the print head with hotend and nozzle, with the material being melted at the hotend. The liquid material is transported to the nozzle, which accelerates the flow and increases the shear of the material due to the cross-sectional diameter d narrowing to usually $d = 0.4$ mm. The high shear rate, particularly in the nozzle, leads to a reduction in viscosity. The viscosity is also

Table 2 Carreau–Yashuda model parameters for PLA

Temperature (°C)	η_0 (Pa)	η_∞ (Pa)	λ (s)	a (−)	n (−)
180	5908.11	− 67.83	0.02706	0.26359	0.69935
190	3297.81	− 723.48	0.06881	0.67835	1.12668
200	2302.04	− 1863.01	0.07427	0.84054	1.30644
210	1519.68	− 6140.73	0.07411	0.95567	1.38260
220	1127.83	− 569950.04	0.03813	0.99955	0.71649

influenced thermally. Higher temperatures lead to lower viscosity. Various approximation functions from the literature are available for the non-Newtonian flow behavior. In addition to the Carreau–Yashuda model [38], this includes the power law model, the Berkley–Herschel model [39] and the Cross-WLF model [40]. From the experimentally determined measurement data, the Carreau–Yashuda model was identified as the best fit for the flow behavior of the PLA material examined. The Carreau–Yashuda model is expressed by the following equation:

$$\eta(\dot{\gamma}) = \eta_\infty + (\eta_0 - \eta_\infty)(1 + (\lambda\dot{\gamma})^a)^{\frac{n-1}{a}}, \tag{11}$$

where η_0 is the zero shear viscosity, η_∞ denotes the infinite-shear viscosity, λ is the time constant related to the fluid's relaxation time, $\dot{\gamma}$ is the shear rate, n is the power law index dictating the degree of shear-thinning behavior, and a is the Yashuda parameter, enhancing the model's flexibility in the transition region. The fitted Carreau–Yashuda model parameters are listed in Table 2.

4.4 Crystallization model

Nakamura model: As the polymer cools down from the molten state, some of its long chains begin to arrange themselves in crystalline structures causing the crystallinity degree of the polymer to increase. Since this process deals with non-isothermal crystallization, the Nakamura equation [41–43] is used to numerically describe the crystallization evolution of the polymer. The equation reads as follows:

$$\frac{\partial \chi_\alpha}{\partial t} = n_\alpha K_\alpha(\theta, \dot{\theta})(1 - \chi_\alpha)\left(\ln\frac{1}{1-\chi_\alpha}\right)^{\frac{n_\alpha - 1}{n_\alpha}}. \tag{12}$$

In this equation, $\partial\chi_\alpha/\partial t$ represents the evolution of the relative crystallinity of the polymer of phase α, n_α is the Avrami coefficient, and K_α is the crystallization rate constant. The crystallization rate constant is described as being dependent on the temperature and the cooling rate presented by the modified Nakamura–Ziabicki model [44] as

$$K_\alpha(\theta) = K_{max,\alpha}(\dot{\theta})\exp\left(\frac{-4\ln(2)(\theta - \theta_{max,\alpha}(\dot{\theta}))^2}{D_\alpha(\dot{\theta})^2}\right). \tag{13}$$

The parameters $K_{max,\alpha}$, D_α and $\theta_{max,\alpha}$ are empirical parameters extracted from the DSC measurements using different cooling rates [18]. The α subscripts imply that the parameters are phase dependent; however, it is to be noted that the equation is solved only where the PLA phase is present. Parameter D_α is described as the half-width of the temperature range where crystallization takes place and $\theta_{max,\alpha}$ as the temperature of the maximum crystallization rate [45]. $K_{max,\alpha}$ is taken as $\ln(2)^{1/n}(1/t_{1/2})$ [46]. In the interface region, the effective crystallinity is taken as the linear interpolation of the phase-specific relative crystallinity.

Fitting of the crystallization parameters for PLA To be able to interpolate between the measured cooling rate, and potentially extrapolate outside the range, Sierra et al. [47] suggested a power function for D_α and $\theta_{max,\alpha}$, and a linear function for $K_{max,\alpha}$:

$$\theta_{max,PLA}(\dot{\theta}) = C_1 \cdot \dot{\theta}^{-C_2}, \tag{14a}$$

$$K_{max,PLA}(\dot{\theta}) = C_3 \cdot \dot{\theta} + C_4, \tag{14b}$$

$$D_{PLA}(\dot{\theta}) = C_5 \cdot \dot{\theta}^{C_6}, \tag{14c}$$

where C_1 to C_6 are the fitting coefficients (shown in Table 3) and $\dot{\theta}$ is the cooling rate in °C/s.

As the increase in crystallinity is an exothermic process, the heat release affects the temperature and should be coupled with the heat transport equation. According to the literature [48], this coupling term is taken to be

$$R = \rho_{PLA}\Delta H_{f,PLA} X_{abs.,PLA}\frac{dX_{PLA}}{dt} \tag{15}$$

which then flows back to the heat equation's solution.

Using the parameters shown in Table 3, validation is achieved by comparing the simulation results for each particular cooling rate with the experimental analysis as shown in Fig. 6.

4.5 Computing effective elastic properties

Solid mechanics model : To compute the stress–strain state in the simulation domain, solid mechanics is considered for the

Table 3 Fitted crystallization parameters

C_1	C_2	C_3	C_4	C_5	C_6
406.49	0.044	0.001	0.0024	9.106	0.569

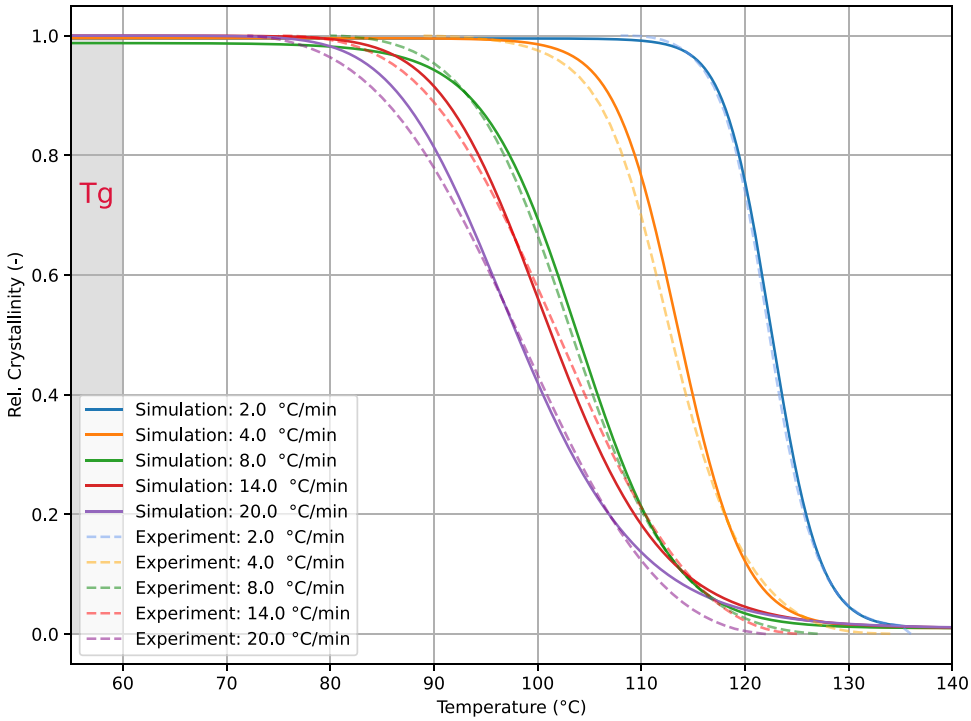

Fig. 6 Relative crystallinity at different cooling rates (2, 4, 8, 14, 20 °C/min). Comparison between experimental and simulation data. Solid lines represent the numerical simulation data, while dashed lines represent the data from the DSC measurements

quasi-static special case, in the absence of body forces. In this context, the balance of linear momentum reads

$$\nabla \cdot \overline{\boldsymbol{\sigma}} = \mathbf{0}, \quad \overline{\boldsymbol{\sigma}} = \sum_{\alpha=1}^{N} \phi_\alpha \boldsymbol{\sigma}^\alpha \tag{16}$$

with $\overline{\boldsymbol{\sigma}}$ denoting the interpolated Cauchy stress based on the phase-specific Cauchy stress tensors $\boldsymbol{\sigma}^\alpha$, cf., e.g., [49] regarding finite deformations. Here, a small strain framework is considered. Regarding the diffuse interface, the infinitesimal strain tensor $\boldsymbol{\varepsilon}$ is assumed to be constituted by the interpolation of the phase-specific $\boldsymbol{\varepsilon}^\alpha$, reading

$$\boldsymbol{\varepsilon} = \sum_{\alpha=1}^{N} \phi_\alpha \boldsymbol{\varepsilon}^\alpha. \tag{17}$$

Taking into account the jump condition approach cf., e.g., [49–51], the phase-specific strains can be written as

$$\boldsymbol{\varepsilon}^\alpha = \boldsymbol{\varepsilon} + \sum_{\delta=1,\delta\neq\alpha}^{N} \phi_\alpha [\boldsymbol{\varepsilon}]^{\alpha\delta}. \tag{18}$$

cf. also Prahs et al. [52, Eq. (11)]. In this regard, the phase-specific strain $\boldsymbol{\varepsilon}^\alpha$ is additively decomposed, into an elastic contribution $\boldsymbol{\varepsilon}^{\mathrm{el},\alpha}$ and a contribution due to the crystallization $\boldsymbol{\varepsilon}^{\chi,\alpha}$, reading

$$\boldsymbol{\varepsilon}^\alpha = \boldsymbol{\varepsilon}^{\mathrm{el},\alpha} + \boldsymbol{\varepsilon}^{\chi,\alpha}, \quad \boldsymbol{\varepsilon}^{\chi,\alpha} = \chi^\alpha \boldsymbol{\varepsilon}^{\chi,\alpha}_{\max}. \tag{19}$$

Here, the volumetric shrinkage due to crystallization is considered to be isotropic and, thus, $\boldsymbol{\varepsilon}^{\chi,\alpha}_{\max} = \varepsilon^{\chi,\alpha}_{\max} \boldsymbol{I}$ holds, with $\varepsilon^{\chi,\alpha}_{\max}$ denoting the phase-specific maximum crystallization shrinkage [53]. Another strain contribution that could be taken into account is the strain due to thermal expansion during the cooling process. However, since the application of this work takes place at room temperature, the thermal strain contribution was not taken into consideration.

The phase-specific stresses are calculated by means of Hooke's law.

$$\boldsymbol{\sigma}^\alpha = \mathbb{C}^\alpha \left[\boldsymbol{\varepsilon}^{\mathrm{el},\alpha}\right] = \mathbb{C}^\alpha \left[\boldsymbol{\varepsilon}^\alpha - \boldsymbol{\varepsilon}^{\chi,\alpha}\right], \tag{20}$$

with $\mathbb{C}^\alpha$ denoting the phase-specific stiffness. In the work at hand, an isotropic stiffness is considered, for brevity, given by $\mathbb{C}^\alpha = 3K^\alpha \mathbb{P}_1 + 2G^\alpha \mathbb{P}_2$. In this context, the phase-specific compression modulus is referred to as K^α and the phase-specific shear modulus as G^α. Morever, the first and second projectors $\mathbb{P}_1 = 1/3\boldsymbol{I} \otimes \boldsymbol{I}$, $\mathbb{P}_2 = \mathbb{I}^{\mathrm{S}} - \mathbb{P}_1$ are introduced. The elastic modulus of PLA changes significantly with temperature. The work of Cao et al. [54] is used as the basis for the PLA's elastic modulus dependency on the temperature. Their plot has been digitized, fitted, and used as an input in the current material model.

Even though the material is assumed to behave in a pure elastic manner, expanding to solid mechanics model in the context of multiphase field has to include plasticity or viscoelasticity been attempted in the literature and can be included in the current workflow in the future. To this end, the authors refer the reader to Prahs et al. [52] for the extension of the solid mechanics model to include plasticity, where it has been successfully used to model microstructure evolution due to

Table 4 Summary of the governing equations

Multiphasefield model
$\dot{\phi}_\alpha = \partial_t \phi_\alpha + \mathbf{u} \cdot \nabla \phi_\alpha = -M \frac{\delta \mathcal{F}}{\delta \phi_\alpha} - \lambda$
Heat transport model
$\frac{\partial \theta}{\partial t} = \frac{1}{\rho c_p} \nabla \cdot (\kappa \nabla \theta) - \mathbf{u} \cdot \nabla(\theta) + \rho_\alpha \Delta H_{c,\alpha} X_{abs.,\alpha} \frac{dX_\alpha}{dt}$
Fluid flow model
$\nabla \cdot \mathbf{u} = 0$
$\rho\left(\frac{\partial \mathbf{u}}{\partial t} + \mathbf{u} \cdot \nabla \mathbf{u}\right) = -\nabla p + \nabla \cdot \left(\mu\left(\nabla \mathbf{u} + (\nabla \mathbf{u})^T\right)\right) + \rho \mathbf{f}_\mathbf{v} + \mathbf{K}$ $\mathbf{K} = -\nabla \cdot \boldsymbol{\Theta} = -2A(\gamma_{12}) \nabla \cdot [(\nabla \phi_1 \otimes \nabla \phi_1)]$
Solid mechanics model
$\nabla \cdot \overline{\boldsymbol{\sigma}} = \mathbf{0}, \quad \overline{\boldsymbol{\sigma}} = \sum_\alpha^N \phi_\alpha \boldsymbol{\sigma}^\alpha$
$\boldsymbol{\varepsilon}^\alpha = \boldsymbol{\varepsilon}^{el,\alpha} + \boldsymbol{\varepsilon}^{\chi,\alpha}, \quad \boldsymbol{\varepsilon}^{\chi,\alpha} = \chi^\alpha \boldsymbol{\varepsilon}^{\chi,\alpha}_{max}$
$\boldsymbol{\sigma}^\alpha = \mathbb{C}^\alpha\left[\boldsymbol{\varepsilon}^{el,\alpha}\right] = \mathbb{C}^\alpha[\boldsymbol{\varepsilon}^\alpha - \boldsymbol{\varepsilon}^{\chi,\alpha}]$
Crystallization Model
$\frac{\partial X_\alpha}{\partial t} = n K_\alpha(\theta, \dot{\theta})(1 - X_\alpha)(\ln \frac{1}{1 - X_\alpha})^{\frac{n_\alpha - 1}{n_\alpha}}$
$K_\alpha(\theta) = K_{max,\alpha}(\dot{\theta}) \exp(\frac{-4 \ln(2)(\theta - \theta_{max,\alpha}(\dot{\theta}))^2}{D_\alpha(\dot{\theta})^2})$

the presence of plastic strains in Kannenberg et al. [55]. As for the inclusion of viscoelasticity within the multiphase-field method using a phase-inherent Maxwell–Wiechert model and mechanical jump conditions, the model proprosed by Schwab et al. [56] can be used.

Numerical homogenization: There exists a multitude of methods for the homogenization of heterogeneous material properties to calculate the effective elastic properties of the structure. The lower and upper bounds represented by Voigt [57] (iso-strain assumption) and Reuss [58] (iso-stress assumption) have been widely regarded as validation for any homogenization scheme since any method should lie between those bounds [59]. In this work, the homogenization scheme for porous media described in Reder et al. [60] is used. This method has been shown to work well in the case of pure elastic material behavior compared to Voigt, Reuss, and second-order Hashin–Shtrinkman bounds [61]. It is to be noted that in the case of viscoelastic material behavior, different homogenization methods could be better suited. For example, Nguyen et al. [62] developed a self-consistent model for modeling of porous media exhibiting viscoelastic material behavior, while Barral et al. [63] used a modified mean-field method (Mori–Tanaka method) for the homogenization of material composites exhibiting both viscoelastic and viscoplastic behavior.

To that end, using [60], the effective Lamé parameters are calculated using the following expressions:

$$2\tilde{\mu} = \frac{3 \cdot \tilde{\boldsymbol{\varepsilon}} \tilde{\boldsymbol{\sigma}} - \mathrm{tr}(\tilde{\boldsymbol{\varepsilon}})\,\mathrm{tr}(\tilde{\boldsymbol{\sigma}})}{3 \cdot \tilde{\boldsymbol{\varepsilon}}^2 - \mathrm{tr}(\tilde{\boldsymbol{\varepsilon}})^2}, \tag{21a}$$

$$\tilde{\lambda} = \frac{1}{3}\left[\frac{\mathrm{tr}(\tilde{\boldsymbol{\sigma}})}{\mathrm{tr}(\tilde{\boldsymbol{\varepsilon}})} - 2\tilde{\mu}\right]. \tag{21b}$$

where $\tilde{\boldsymbol{\sigma}}$ and $\tilde{\boldsymbol{\varepsilon}}$ are the volume averaged values of the stress and the strain, respectively, computed over the whole domain Ω using

$$\tilde{\boldsymbol{\sigma}} = \frac{1}{\Omega} \int_\Omega \boldsymbol{\sigma}\, \mathrm{d}V, \quad \tilde{\boldsymbol{\varepsilon}} = \frac{1}{\Omega} \int_\Omega \boldsymbol{\varepsilon}\, \mathrm{d}V. \tag{22}$$

4.6 Summary

Governing equations: The governing equations considered for modeling the physical processes taking place in the PLA filament as it cools down are summarized in Table 4 for better readablity. The convective form of the order parameter evolution is used to couple the Navier–Stokes equation with the phase-field model. The heat transport equation is used in its generalized form to model the heat conduction and convection in the PLA filament as it cools down. The Nakamura equation in its differential form is used to model the evolution of crystallinity in the polymer, while the equation of momentum balance as well as Hooke's law are used to calculate the resulting stresses due to the elastic and inelastic strains. The list of material parameters used is shown in Table 5.

Table 5 Summary of all model and material parameters

Parameter	Value	Unit
Thermal properties		
Thermal conductivity (κ)		
PLA	0.160 [64]	W°C/m
Air	0.026 [65]	W°C/m
Specific heat capacity (C_p)		
PLA	Temperature-dependent (Fig. 4)	J/(g·°C)
Air	1 [66]	J/(g·°C)
Density (ρ)		
PLA	1240 [67]	kg/m^3
Air	1 [68]	kg/m^3
Crystallization enthalpy (ΔH_c)	1.3 (Table 1)	J/g
Absolute crystallinity ($X_{abs.}$)	1.8 (Table 1)	%
PLA crystallinity properties		
T_{max}	Eq. 14a	K
D	Eq. 14c	K
K_{max}	Eq. 14b	s^{-1}
Fluid flow parameters		
Dynamic viscosity (μ)		
PLA	Carreau–Yashuda model (Table 2)	Pas
Air	1.75x10^{-5} [69]	Pas
Surface tension $\gamma_{\alpha\beta}$	41.6 [70]	mN/m
Solid mechanics parameters		
Elastic modulus of PLA	Digitized from [54]	GPa
Poisson's ratio (ν) of PLA	0.38 [71]	-
Volumetric crystallization shrinkage (ε_{max}^{PLA})	0.5 [72]	%
Numerical parameters		
Mesh size	10	μm
Time step	0.001	s
Diffuse interface width	7	Cells

5 Simulation studies and discussions

5.1 Numerical simulation workflow

The material properties are derived, either experimentally or analytically, and are used as input parameters to the PACE3D solver, as well as the user parameters which represent the process parameters. The domain is filled with the air phase, then an iterative process takes place, where (1) the PLA phase is filled into the simulation domain in a predetermined position depending on its row and column number, with initial temperature and properties as specified in the input, and (2) this newly filled layer is simulated using the numerical models presented above. The deposited filament's form does not take into account the change in form due to the extrusion in the nozzle, and hence an ideal elliptical/spherical form is assumed. This process is repeated until the number of layers (rows and columns) defined by the user has been simulated. The output of this process is a finalized structure upon which loading simulations can be conducted and postprocessing tools for the analysis for physical and structural properties can be used. Then the domain is cut in both directions so that the PLA phase touches the borders. This new domain is important to have, as it will be used next in the mechanical loading simulation, since it allows the loading to be applied on the PLA phase and not on air. The output of the loading simulation is used to calculate the effective Young's modulus as well as the porosity.

5.2 Single-layer study

Firstly, the working model is illustrated in detail by simulating one PLA filament in 2D as an example. The geometry of the layer is set to be 400 × 200 µm with an initial temperature of 200 °C, bed temperature of 60 °C and environment initial temperature of 150 °C. The starting point of the simulation refers to the moment when the filament hits the bed. The filament is assumed to have a homogeneous temperature distribution with the value of the nozzle temperature. To better illustrate the effect of the viscous flow,

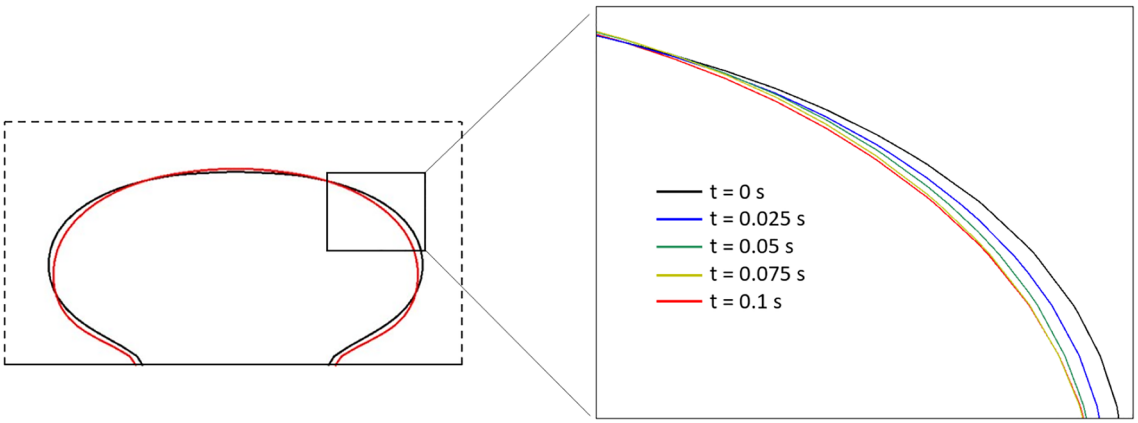

Fig. 7 Cross-sectional form change after deposition at different times. The form changes with time—the filament flows and relaxes on the bottom boundary

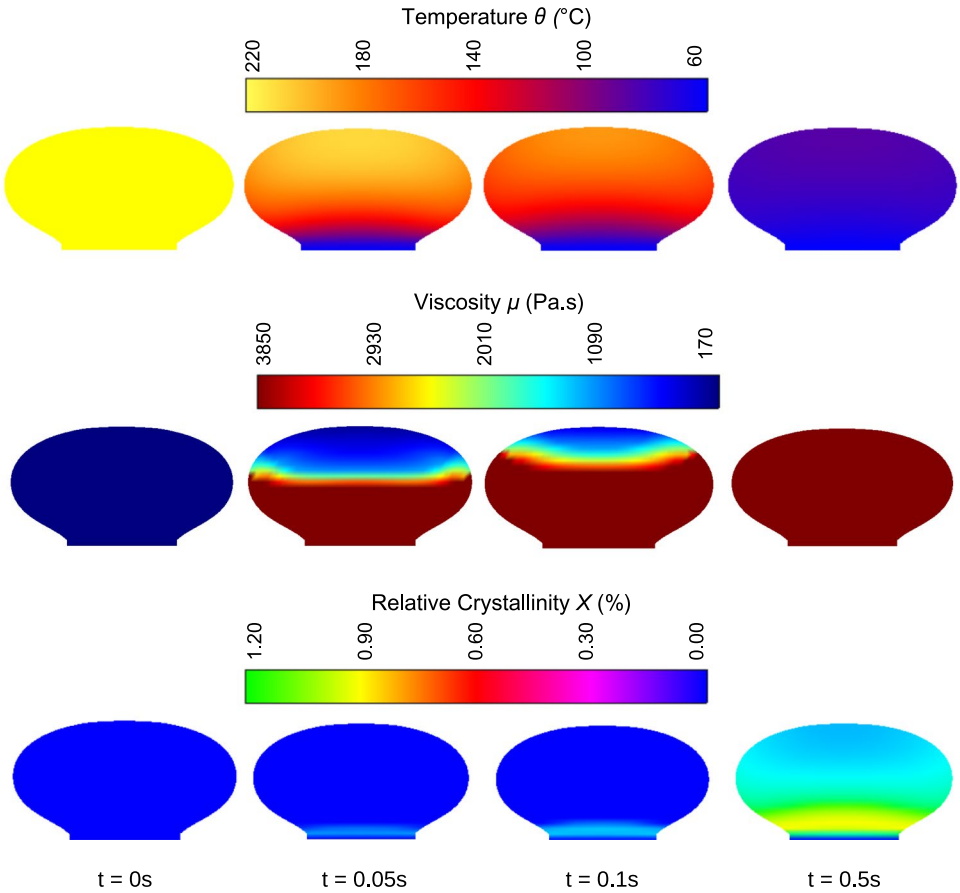

Fig. 8 Evolution of the temperature (top), viscosity (middle) and relative crystallinity (bottom) fields at times $t = 0, 0.05, 0.1, 0.5s$

a filament with a lower viscosity has been used (168 Pa s for 220 °C up to 3842 Pa s for 180 °C) (see Appendix 16).

Figure 7 shows the contour shape of the PLA deposit at the start of the simulation and at different time steps during the simulation. A visible change in form can be observed, characterized by a flattening of the deposit, an increasing contact area with the bed, and contracting of the sides as shown in the zoomed figure of the boundary. Such flattening is the expected behavior of the extruded filament as simulated by Lei et al. [20].

The temperature, viscosity and relative crystallinity distribution plots are shown in Fig. 8 for different times. The filament cools down from the bottom (in contact with the bed) upward, from its initial temperature until almost the

whole filament reaches the bed temperature. The temperature distribution within the domain significantly influences both the viscosity and the relative crystallinity distribution of the filament. Initially, the viscosity is low at 168 Pas due to the high temperature (220 °C). As the filament cools, the viscosity increases from the bottom up, mirroring the temperature decrease. This rapid cooling affects the filament's flow, occurring predominantly at the start of the simulation. Shortly after, the filament becomes too rigid to flow further. Temperature also greatly impacts the crystallinity behavior within the filament. When the temperature is high, no crystallization occurs. As the filament cools, crystallization begins, but this process is uneven due to the non-uniform cooling. Despite this, the relative crystallinity values remain very low because the high cooling rate effectively suppresses the polymer's crystallization.

Furthermore, using another simulation with initial temperature of 210 °C, a plot of the temperature evolution with time along with the cooling rate at the middle point of the layer is shown in Fig. 9 (left). The filament cools down to 62 °C within the duration of the simulation (1 s), with an average cooling rate (taken as $(T_{nozzle} - T_{bed})/t_{cooling}$) of 150K/s, while at the start it could go as high as 700K/s. Figure 9 (right) shows a magnification of the initial profile of the temperature evolution of the filament depending on selected process parameters variation [28], as well as the temperature evolution of the current study. It can be observed that the cooling behavior fits well to the currently used temperature model.

5.3 Multiple layers study

Description of case studies: As the dynamics of the model has been illustrated on one layer, the attention is shifted to multiple layer simulations. This is carried out by sequentially simulating layer by layer till completion and is shown in Fig. 10. In the figure, the blue colored shapes display potential places for the layers to be deposited on as calculated by the algorithm, while the black lines mark the initial state of the simulated layer and red color is the state at the end of the simulation of that layer. The algorithm prints the layers from left to right, bottom to top as shown by the numbers.

A grid of 3×3 of deposited PLA filaments in 2D was simulated using the outlined procedure above. Six cases were considered in the simulation study where the process

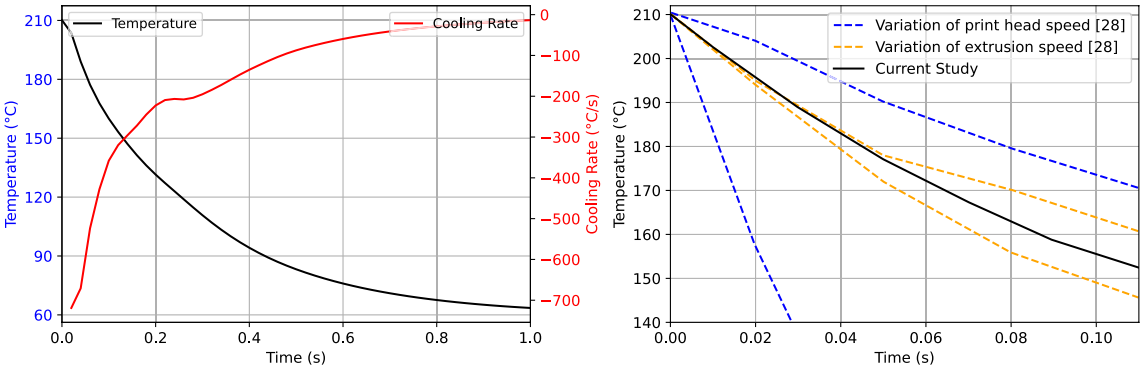

Fig. 9 Temperature evolution analysis. Left: temperature (black line) and cooling rate (red line) evolution in the one-layer simulation study. Right: comparison and validation between the temperature evolution in the current study and the literature [28]

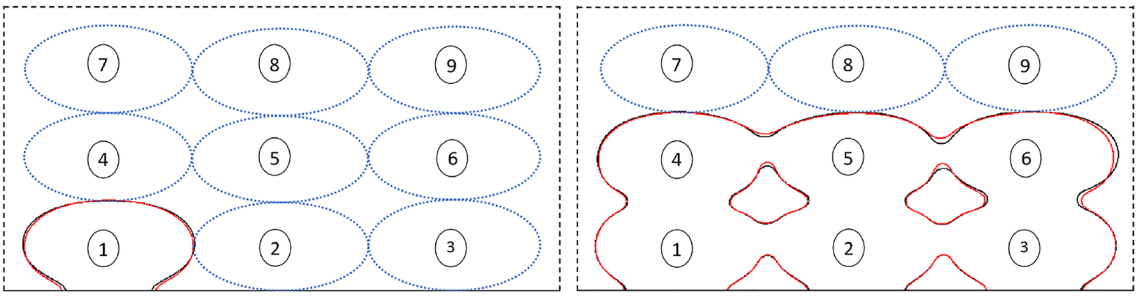

Fig. 10 Printing sequence and evolution of the morphologies of the first (left) and sixth (right) layers, where solid black and red lines represent the initial and final state, respectively, while the dotted red lines show the potential positioning of the next layers as determined by the filling algorithm

parameters were varied. The considered process parameters were the nozzle temperature, bed temperature, layer height, and filament type. To investigate the effect of the filament viscosity, the filament properties used in the one-layer study was considered as "Low Viscosity" while the one investigated in Sec. 3.1 was considered as "High Viscosity". Two boundary values for the nozzle temperature were used: 220 and 180 °C, and for the bed temperature 60 and 75 °C. To investigate the effect of layer height, two values were considered as well. Two typical layer heights used during printing are 200 and 320 µm (corresponding to 50 % and 80 %of a typical nozzle diameter of 0.4 mm, respectively). Finally, a reference case was established where no temperature evolution, fluid flow, or crystallization was allowed to take place. This corresponds to a purely geometrical configuration of layers. Table 6 outlines the simulations studied in this work.

Table 6 Summary of investigated process parameters

Case	Filament Type	Nozzle Temp. (°C)	Bed Temp. (°C)	Layer Height (µm)
1	Low Viscosity	220	60	200
2	Low Viscosity	180	60	200
3	High Viscosity	220	60	200
4	Low Viscosity	220	75	200
5	Low Viscosity	220	60	320
6	Reference	–	–	200

Discussion of the results

Figure 11 shows the final microstructure of the 6 simulated cases. The same flowing behavior observed in Fig. 7 is evident as well, with filaments displaying a degree of flattening influenced by the initial temperature values and filament type. Cases 1 and 2 demonstrate the effect of nozzle

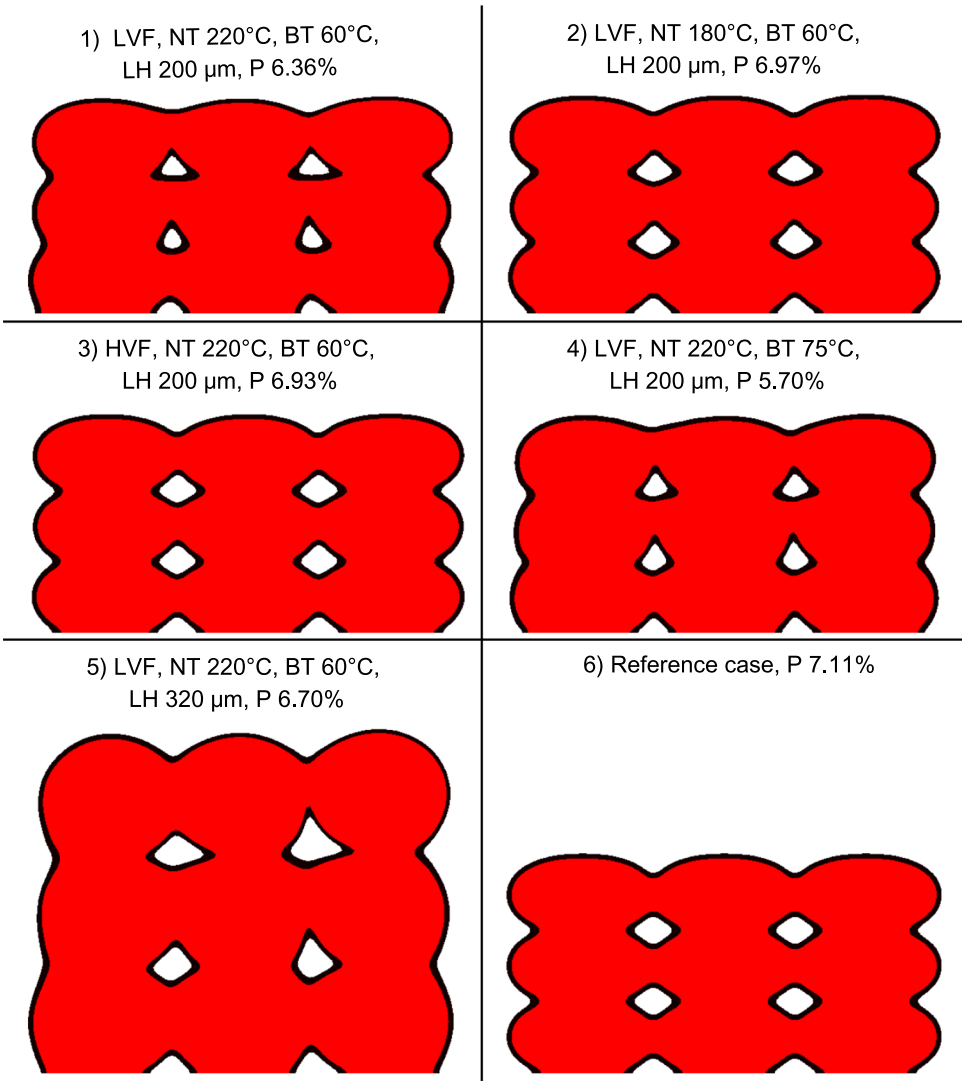

Fig. 11 Final microstructure of the cases investigated. Process parameters for each case is shown for reference, where L/HVF stands for low/high viscosity filament, NT for nozzle temperature, BT for bed temperature, LH for layer height and P for porosity

temperature on the viscous flow of the filament and, consequently, on the shape of the pores. The higher-temperature case (Case 1) exhibits more viscous flow compared to the lower-temperature case (Case 2). Additionally, increasing the bed temperature (Case 4) allows the filament to flow more, as it decreases the cooling rate and keeps the filament in the flow regime longer.

By changing the filament, despite the different nozzle temperatures, the difference in flow between Case 2 and Case 3 appears to be minimal, both in the shape of the layers and the pores. This can be attributed to the fact that it is the corresponding viscosity, rather than the temperature value itself, that plays a crucial role. Since the filaments in both cases exhibit different viscosity–temperature relationships, similar results can be achieved with different temperature values.

Increasing the layer height (Case 5) results in the most distortion in the pore shapes. More flowing is supported due to the larger layer volume as well as the slower cooling rate that takes place as the volume increase.

In scenarios where the temperature is low (and viscosity is high), the pores tend to possess a uniform diamond shape, primarily produced by the geometric alignment of the filaments, as confirmed in Case 6. Conversely, when the filament's ability to flow increases (due to lower viscosity), the pores assume a distinct asymmetrical diamond shape [73].

Although increasing the layer height resulted in the most distortion in pore shapes, it had little impact on porosity, which was calculated to be 6.70 %. For reference, the porosity of the baseline case was 7.11 %. Increasing the bed and nozzle temperature, as well as using a low-viscosity filament, produced the lowest porosity. The differences in flow behavior significantly affect porosity, which in turn influences the elastic modulus, a relationship that will be investigated further.

For further illustrations, the temperature history in the midpoint of the second layer deposit is plotted for cases 1 and 2, where the initial temperature was 220 and 180 °C (Fig. 12). Visible temperature increases appear whenever a new layer is deposited. The highest increase in temperature occurred as the layers directly on top of it are deposited. This increase has the value of 27 °C for Case 1 and 20 °C for Case 2. The rest of the layers have a diminishing effect with the difference between both cases getting more negligible.

In Fig. 13, the hydrostatic component of the strain (representing the volume change) are presented along with the relative crystallinity distribution for Case 3. The hydrostatic component is calculated as $\mathrm{tr}(\bar{\varepsilon})/3$. The crystallization distribution within the domain is highly inhomogeneous, with the highest degrees of relative crystallinity found in the middle layers. The bottom layers cool extremely fast due to their contact with the bed, limiting their ability to crystallize despite having the longest exposure time. In contrast, the middle layers exhibit the highest relative crystallinity, as

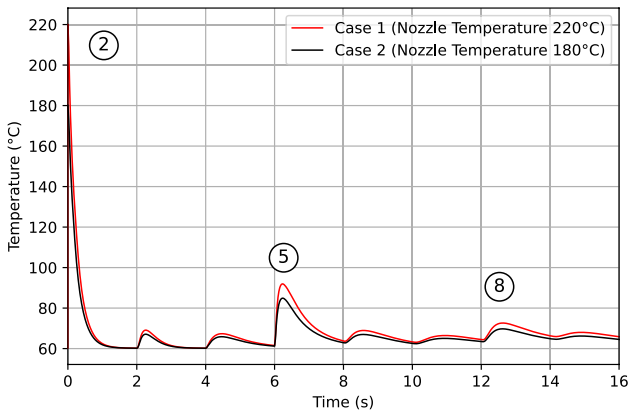

Fig. 12 Temperature history analysis of layer 2 (center-bottom) during the whole simulation for the low-viscosity filament with 220 and 180 °C nozzle temperature simulation studies

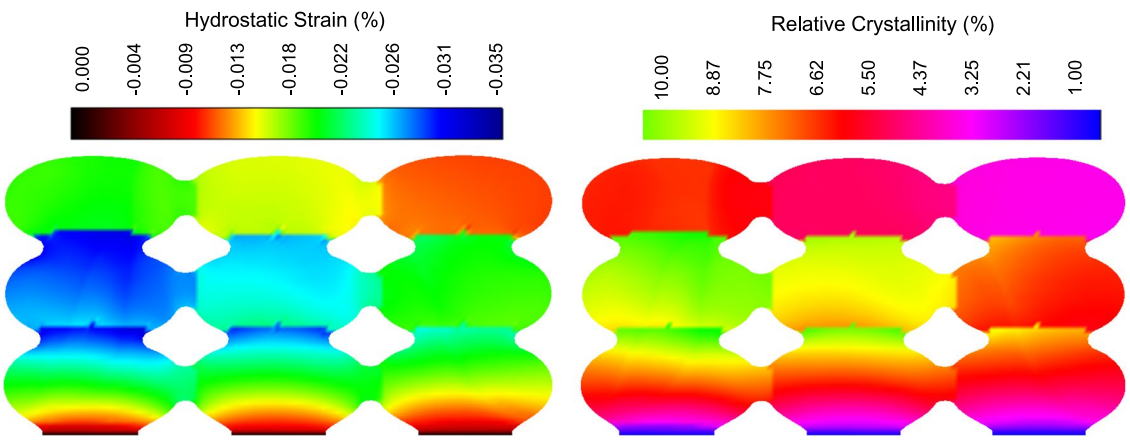

Fig. 13 Comparison between hydrostatic strain (left), and relative crystallinity (right) for Case 3

their cooling rate is relatively slower. Additionally, the subsequent deposition of top layers reheats the middle layers, promoting further crystallization. The top layers show the least relative crystallinity. A general trend can be observed where crystallinity decreases from left to right, starting from the middle layer. This is primarily due to the varying duration the strand is exposed to high temperatures. It is hypothesized that if further deposition were to occur, the crystallinity of these top layers would increase to match that of the middle layers. Overall, despite the inhomogeneity, the degree of relative crystallinity remains very low throughout the filament, with a domain-averaged relative crystallinity of 5.70 %, and the absolute crystallinity would then be even lower. As discussed in Sect. 4.5, the only contribution to the inelastic strains is due to crystallization, which is compressive in nature as the polymer shrinks during this process. This shrinkage however is shown to be minimal where the maximum shrinkage due to crystallization is 0.035 % occuring in the areas where the crystallinity is highest.

5.4 Mechanical loading simulations

Description of the algorithm: After simulating the final structure in the previous step, a mechanical loading simulation is conducted to determine the effective Young's modulus of the structure. To ensure that the load is applied directly to the PLA phase and not to the air phase, the domain is cut so that the PLA phase directly touches the borders of the domain. The loading boundary conditions are set with orthogonal displacement-controlled loading on the top and bottom boundaries (in the Y-direction), while the right and left boundaries are stress-free. The temperatures of the filaments and surroundings were set to room temperature (25 °C), mimicking realistic tensile experiments. Subsequently, the corresponding effective Young's modulus of the simulated structure is determined using Eq. 21. For better comparability of the Young's modulus with other studies, the calculated effective Young's modulus is normalized with the Young's modulus at room temperature (2.56 GPa for this study, however the Young's modulus from the corresponding case in the literature has been used to normalize their results).

Analysis on the stresses and strains distribution: Figure 14 illustrates the strain and stress distributions in the Y-direction for Case 3, where the porosity is 6.93 %. The distributions reveal higher stress and strain values at the vertical necks between the layers. The highest strains are observed along the inner edges of the pores. Additionally, the middle column experiences the highest stress, as the right and left columns are subjected to stress-free boundary conditions. This distribution pattern indicates critical areas where the material is most likely to experience mechanical failure under loading conditions. It also shows the non-load-bearing nature of the pores and how it forms stress-concentration sites within the microstructure. Further studies focusing on the failure behavior of PLA along with a visco-elasto-plastic material model could be conducted as an extension to this model.

Analysis of the effect of process parameters on the porosity and effective elastic modulus: Table 7 shows the resulting porosities along with the normalized Young's modulus. A clear dependence of the Young's modulus on the process parameter can be observed. As the flow ability of the filament increases, the porosity decreases and subsequently the volume of full material increases. This leads to a higher Young's modulus compared to cases where the porosity is high. Therefore, the highest Young's modulus is calculated from Case 4, where a low filament viscosity was used along with a higher nozzle and bed temperature, while the lowest Young's modulus is calculated from the reference case. The calculated porosity and Young's modulus can also be linearly fitted within the porosity range investigated as shown in Fig. 15. The diagram contains experimental data from the literature [74, 75] as well, where the Young's moduli for

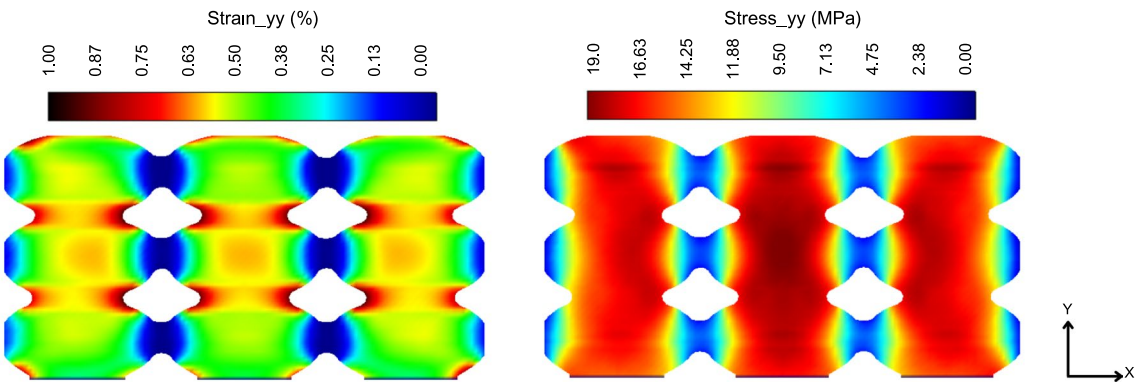

Fig. 14 Strain and stress distributions in the Y-direction during the mechanical loading simulation. The microstructure corresponds to that of Case 3

Table 7 Summary of simulations results showing porosity and the normalized Young's modulus

Case	Filament type	Nozzle Temp. (° C)	Bed Temp. (° C)	Layer height (μm)	Porosity (%)	Normalized Young's modulus
1	Low viscosity	220	60	200	6.36	0.83
2	Low viscosity	180	60	200	6.97	0.80
3	High viscosity	220	60	200	6.93	0.80
4	Low viscosity	220	75	200	5.70	0.85
5	Low viscosity	220	60	320	6.70	0.81
6	Reference	–	–	200	7.11	0.78

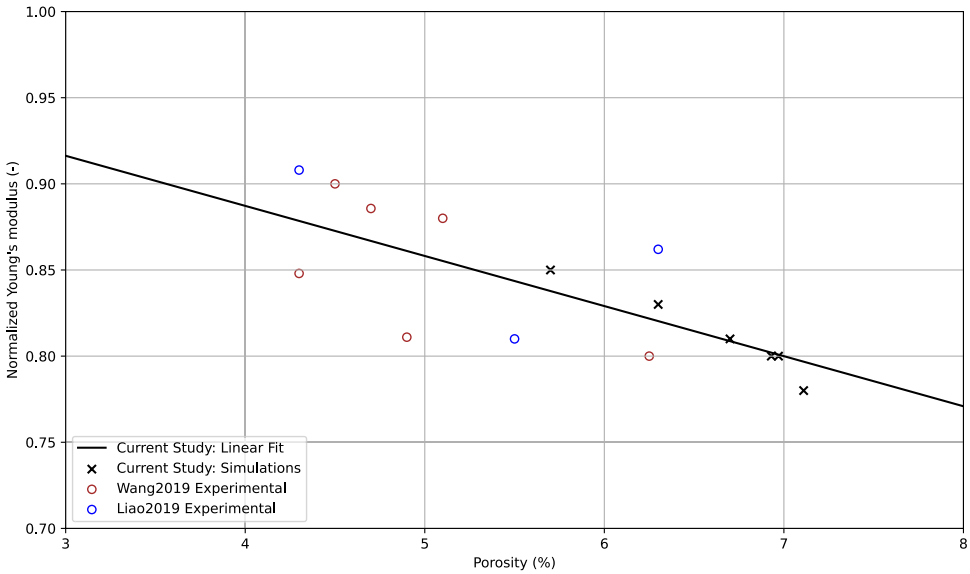

Fig. 15 Effect of porosity on effective elastic modulus compared with the literature. Colored dots represent experimental data from the literature and black dots are the simulation studies from the current work. The black line relates to the fitting curve from the current work

different porosities have been compared. Even beyond the range of porosities simulated in this study, good agreement is found as the model is able to predict the experimental results with an average accuracy of 3.6 % and maximum error of around 4.8 %. Hence, given a known porosity, the elastic modulus can be estimated and vice versa.

Limitations: Various reasons could contribute to the discrepancies between experimental values from the literature and simulation results from the current study. One primary factor is the inherent variability in polymer strains, leading to statistical differences between tests within the same study as well as across different studies. Moreover, the interfacial strength between the layers was not taken into consideration. This, however, plays an important role in the mechanical properties of the final structure [76]. Additionally, the simulation fits assumed that only geometry affects the elastic modulus. However, the degree of crystallinity, which significantly impacts mechanical properties, was not considered. In this study, the evolution of crystallinity was deemed negligible, and the filament was initially assumed to be totally amorphous. Realistically, though, the polymer undergoes some degree of flow-induced crystallization during extrusion from the nozzle [77, 78]. Moreover, the model assumes a linear elastic behavior, whereas a viscoelastic material behavior is more realistic for the polymer. Finally, the temperature dependent specific heat capacity would depend on the cooling rate, however this would not taken into consideration for this study. This is also true for the polymer shrinkage coefficient which depends heavily on the cooling rate, but was assumed to be constant. Finally, there is no direct validation between the simulated microstructure and porosity based on the specific process parameters (such as nozzle and bed temperature) from the experiments. Instead, porosity was chosen as the primary identifying

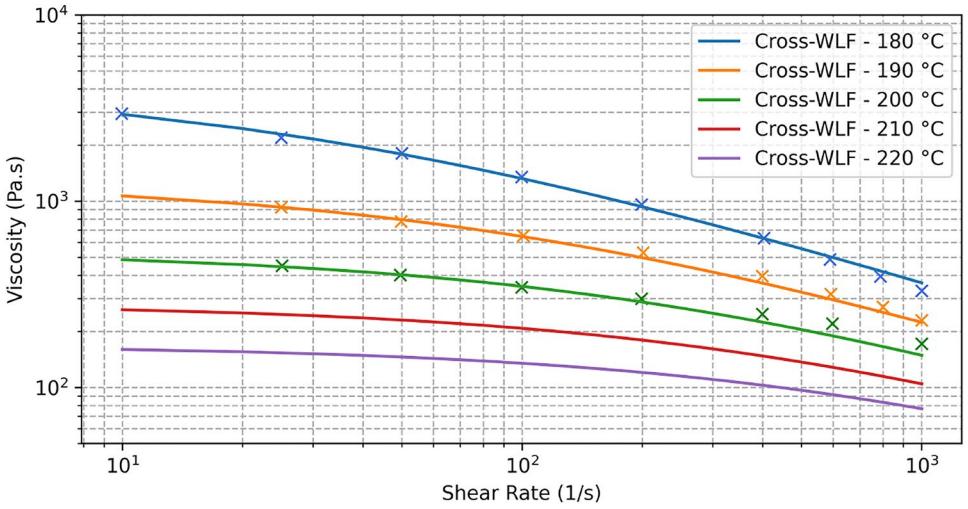

Fig. 16 Cross-WLF model for the low-viscosity filament

feature, and a direct comparison was made between the simulated and experimentally obtained porosity values and their correlation to Young's modulus.

6 Conclusion and outlook

In this work, a comprehensive workflow was presented to simulate the filament flow immediately after extrusion, the temperature and crystallization evolution, the development of residual stresses, and the calculation of the effective Young's modulus and porosity. The simulation studies demonstrated the impact of temperature and viscosity on the viscous flow of the filaments. At higher temperatures and lower viscosities, filaments exhibit a flattening and shrinking behavior, altering the shape and area of the pores between them, while at lower temperatures and higher viscosities, the filament becomes too rigid and little alteration to the pores' shapes is observed.

The very high cooling rates lead to the suppression of crystallinity within the filament. To understand the effect of crystallinity on the effective mechanical properties, simulations of different semi-crystalline polymers and varying cooling rates could be conducted. Changes in porosity within the printed structure directly affect the mechanical properties, as pores are non-load-bearing and thus reduce the effective Young's modulus of the entire structure. This correlation was shown to be linear within the range of porosities investigated.

More work could be done to address the limitations addressed above. Nevertheless, the developed model and its workflow offer the versatility to incorporate such material properties with ease and to work with a wide range of materials, provided the necessary parameters are available.

Appendix A

A.1 Viscosity analysis for the "low-viscosity filament"

Experimental procedure: Viscosity measurements using HCV were done on another PLA filament with the color red. However since HCV can only deliver apparent viscosities, there exists inaccuracies in these measurements which cannot be determined unless a plate–plate rheometer was used afterward. However, the values were found to be within the range of PLA filament viscosities found in the literature [23, 79–82].

Analytical analysis: The Cross-WLF model, similar to the Carreau–Yasuda model, is designed to describe the viscosity behavior of shear-thinning polymers. The viscosity as a function of shear rate and temperature is calculated using

$$\eta(\dot{\gamma},T)=\frac{\eta_0}{1+\frac{\eta_0\cdot\dot{\gamma}}{\tau^*}^{1-n}},\quad \text{with}\quad \eta_0=D_1\cdot\exp\left(\frac{-A_1\cdot(T-T^*)}{A_2+T-T^*}\right). \tag{A1}$$

In Eq. (A1) η_0 represent the zero shear viscosity (viscosity at zero shear rate and temperature T), τ^* the critical shear stress, a characteristic stress level at which the transition from Newtonian to shear-thinning behavior occurs, T^* the glass transition temperature, A_1 and A_2 are empirical fitting parameters, D_1 a reference viscosity at a shear rate of zero and at the temperature T^* and n a dimensionless parameter (flow index) indicating the degree of shear-thinning behavior. Figure 16 shows the experimental data as well as the fitted Cross-WLF model. The used parameters are in Table 8.

Table 8 Cross-WLF model parameter values for the low-viscosity PLA filament

A_1	A_2	D_1	τ^*	T^*	n
12.9664	29.3561	1119210	130597	157.956	0.319023

Acknowledgements This research was supported by the "Central Innovation Programme for SMEs" (Zentrales Innovationsprogramm Mittelstand) of the BMWi as part of the FuE Cooperation Project, project number 16KN095324, as well as project number 16KN095321. The authors also gratefully ackowledge the financial support of the MSE programme (no. 43.31.01) of Helmholtz association, Federal Ministry of Education and Research of Germany in the framework of "DASEA-4-SOFC" (no. 05M2022).

Funding Open Access funding enabled and organized by Projekt DEAL.

Data availability Data will be made available upon request.

Declarations

Conflict of interest The authors declare that they have no known competing financial interests or personal relationships that could have appeared to influence the work reported in this paper.

References

1. Hull CW Apparatus for production of three-dimensional objects by stereolithography. U.S. Patent 4 575 330. Patent number: 4 575 330 (1986)
2. Crump SS Apparatus and method for creating three-dimensional objects. U.S. Patent No. 5,121,329. Patent number: 5,121,329 (1992)
3. Paulo A, Santos J, Rocha J, Lima R, Ribeiro J Mechanical properties of pla specimens obtained by additive manufacturing process reinforced with flax fibers **7**(1), 27 https://doi.org/10.3390/jcs7010027
4. Bazyar MM, Tabary SAAB, Rahmatabdi D, Mohammadi K, Hashemi R A novel practical method for the production of functionally graded materials by varying exposure time via photocuring 3d printing **103**, 136–143 https://doi.org/10.1016/j.jmapro.2023.08.018
5. Bellehumeur C, Li L, Sun Q, Gu P (2004) Modeling of bond formation between polymer filaments in the fused deposition modeling process. Journal of Manufacturing Processes 6:170–178
6. Wang J, Xie H, Weng Z, Senthil T, Wu L (2016) A novel approach to improve mechanical properties of parts fabricated by fused deposition modeling. Materials and Design 105:152–159
7. Al-Maharma AY, Patil SP, Markert B Effects of porosity on the mechanical properties of additively manufactured components: a critical review **7**(12), 122001 https://doi.org/10.1088/2053-1591/abcc5d
8. Sun Q, Rizvi GM, Bellehumeur CT, Gu P (2008) Effect of processing conditions on the bonding quality of fdm polymer filaments. Rapid Prototyping Journal 14(2):72–80
9. Pang, R., Lai, M.K., Ismail, K.I., Yap, T.C.: The effect of printing temperature on bonding quality and tensile properties of fused deposition modelling 3d-printed parts **1257**(1), 012031 https://doi.org/10.1088/1757-899x/1257/1/012031
10. Ulkir O, Ertugrul I, Ersoy S, Yağımlı B The effects of printing temperature on the mechanical properties of 3d-printed acrylonitrile butadiene styrene **14**(8), 3376 https://doi.org/10.3390/app14083376
11. Chacón JM, Caminero MA, García-Plaza E, Núñez PJ (2017) Additive manufacturing of pla structures using fused deposition modelling: Effect of process parameters on mechanical properties and their optimal selection. Materials and Design 124:143–157
12. Wu W, Geng P, Li G, Zhao D, Zhang H, Zhao J (2015) Influence of layer thickness and raster angle on the mechanical properties of 3d-printed peek and a comparative mechanical study between peek and abs. Materials 8(9):5834–5846. https://doi.org/10.3390/ma8095271
13. Khatwani J, Srivastava V Effect of process parameters on mechanical properties of solidified pla parts fabricated by 3d printing process. In: Kumar, L., Pandey, P., Wimpenny, D. (eds.) 3D Printing and Additive Manufacturing Technologies. Springer, Singapore (2019). Chap. 9. https://doi.org/10.1007/978-981-13-0305-0_9
14. Holm ES Additive manufacturing process parameter effects on the mechanical properties of fused filament fabrication nylon. Theses and dissertations, Air Force Institute of Technology (2016). https://scholar.afit.edu/etd/398
15. Ning F, Cong W, Hu Y, Wang H (2017) Additive manufacturing of carbon fiber-reinforced plastic composites using fused deposition modeling: Effects of process parameters on tensile properties. Journal of Composite Materials 51:451–462
16. Christiyan KGJ, Chandrasekhar U, Venkateswarlu K A study on the influence of process parameters on the mechanical properties of 3d printed abs composite. In: IOP Conference Series: Materials Science and Engineering, vol. 114, p. 012109 (2016).https://doi.org/10.1088/1757-899X/114/1/012109 . IOP Publishing
17. Alafaghani A, Qattawi A, Alrawi B Experimental optimization of fused deposition modelling processing parameters: A design-for-manufacturing approach. Procedia Manufacturing 10, 791–803 (2017) https://doi.org/10.1016/j.promfg.2017.07.079
18. Descher S Modeling and simulation of crystallization processes in polymer melt flows. Ph.d. dissertation, University of Kassel, Kassel, Germany (2020). https://doi.org/10.17170/kobra-202011022043
19. Lee A, Wynn M, Quigley L, Salviato M, Zobeiry N Effect of temperature history during additive manufacturing on crystalline morphology of peek. Advances in Industrial and Manufacturing Engineering 4, 100085 (2022) https://doi.org/10.1016/j.aime.2022.100085
20. Lei M, Wei Q, Li M, Zhang J, Yang R, Wang Y Numerical simulation and experimental study the effects of process parameters on filament morphology and mechanical properties of fdm 3d printed pla/gnps nanocomposite. Polymers 14, 3081 (2022) https://doi.org/10.3390/polym14153081
21. Lepoivre A, Boyard N, Levy A, Sobotka V Heat transfer and adhesion study for the fff additive manufacturing process. Procedia Manufacturing 47, 948–955 (2020) https://doi.org/10.1016/j.promfg.2020.04.291 . 23rd International Conference on Material Forming
22. Tichý T, Šefl O, Veselý P, Dušek K, Bušek D Mathematical modelling of temperature distribution in selected parts of fff printer during 3d printing process. Polymers **13**(23) (2021) https://doi.org/10.3390/polym13234213
23. Mishra, A.A., Momin, A., Strano, M., al.: Implementation of viscosity and density models for improved numerical analysis of melt flow dynamics in the nozzle during extrusion-based additive

manufacturing. Progress in Additive Manufacturing 7, 41–54 (2022)
24. Šeta B, Sandberg M, Brander M, Mollah MT, Pokkalla D, Kumar V, Spangenberg J Modeling fiber orientation and strand shape morphology in three-dimensional material extrusion additive manufacturing. Composites Part B: Engineering 266, 110957 (2023) https://doi.org/10.1016/j.compositesb.2023.110957
25. Zhou M, Si L, Chen P, al Experimental investigation and numerical simulations of temperature and morphology in material extrusion additive manufacturing. International Journal of Advanced Manufacturing Technology 119, 4863–4876 (2022) https://doi.org/10.1007/s00170-022-08663-w
26. Brandt N, Griem L, Herrmann C, Schoof E, Tosato G, Zhao Y, Zschumme P, Selzer M (2021) Kadi4mat: A research data infrastructure for materials science. Data Science Journal. https://doi.org/10.5334/dsj-2021-008
27. Hötzer J, Reiter A, Hierl H, Steinmetz P, Selzer M, Nestler B (2018) The parallel multi-physics phase-field framework Pace3D. J. Comput. Sci. 26:1–12
28. Kristmann C Numerische und analytische Untersuchung von Strömungsvorgängen beim 3D-Druck unter Berücksichtigung des nicht-newtonschen Fließverhaltens. Unpublished Bachelor thesis, Hochschule Karlsruhe (2023)
29. Prahs A, Reder M, Schneider D, Nestler B (2023) Thermomechanically coupled theory in the context of the multiphase-field method. International Journal of Mechanical Sciences 257:108484
30. Nestler B, Garcke H, Stinner B (2005) Multicomponent alloy solidification: phase-field modeling and simulations. Physical Review E 71(4):041609. https://doi.org/10.1103/PhysRevE.71.041609
31. Jacqmin D (1999) Calculation of two-phase navier-stokes flows using phase-field modeling. Journal of Computational Physics 155(1):96–127. https://doi.org/10.1006/jcph.1999.6332
32. Lowengrub, J., Truskinovsky, L.: Quasi–incompressible cahn–hilliard fluids and topological transitions. Proceedings of the Royal Society of London. Series A: Mathematical, Physical and Engineering Sciences 454(1978), 2617–2654 (1998) https://doi.org/10.1098/rspa.1998.0273
33. Daubner S, Hoffrogge PW, Minar M, Nestler B (1995) Triple junction benchmark for multiphase-field and multi-order parameter models. Comput Mater. 219:11. https://doi.org/10.1016/j.commatsci.2022.111995
34. Kim J, Lowengrub J (2005) Phase field modeling and simulation of three-phase flows. Interfaces Free Bound. pp 435–466
35. Reder M, Hoffrogge PW, Schneider D, Nestler B (2022) A phase-field based model for coupling two-phase flow with the motion of immersed rigid bodies. Int J Numer Methods Eng 123(16):3757–3780. https://doi.org/10.1002/nme.6988
36. Hohenberg PC, Halperin BI (1977) Theory of dynamic critical phenomena. Rev. Mod. Phys. 49:435–479. https://doi.org/10.1103/RevModPhys.49.435
37. Nestler B, Wendler F, Selzer M, Stinner B, Garcke H (2008) Phase-field model for multiphase systems with preserved volume fractions. Phys Rev E 78(1):011604. https://doi.org/10.1103/PhysRevE.78.011604
38. Bird RB, Armstrong RC, Hassager O (1987) Dynamics of Polymeric Liquids Vol 1, 2nd Ed: Fluid Mechanics. John Wiley and Sons Inc, United States. http://inis.iaea.org/search/search.aspx?orig_q=RN:18088690
39. Herschel WH, Bulkley R (1926) Konsistenzmessungen von Gummi-Benzollösungen. Colloid Polym. Sci. 39(4):291–300
40. Hofstätter T, Pimentel R, Pedersen D, Mischkot M, Hansen H Simulation of a downsized fdm nozzle. (2015)
41. Nakamura KG, Watanabe T, Katayama K, Amano T (1972) Some aspects of nonisothermal crystallization of polymers. i. relationship between crystallization temperature, crystallinity, and cooling conditions. J Appl Polym Sci 16:1077–1091
42. Nakamura KG, Katayama K, Amano T (1973) Some aspects of nonisothermal crystallization of polymers. ii. consideration of the isokinetic condition. J Appl Polym Sci 17:1031–1041
43. Nakamura K, Watanabe T, Amano T, Katayama K (1974) Some aspects of nonisothermal crystallization of polymers. iii. crystallization during melt spinning. J Appl Polym Sci 18(2):615–623. https://doi.org/10.1002/app.1974.070180223
44. Ziabicki A (1976) Fundamentals of fibre formation: the science of fibre spinning and drawing. Wiley, London; New York
45. Brucato V, Crippa G, Piccarolo S, Titomanlio G (1991) Crystallization of polymer melts under fast cooling. i: nucleated polyamide 6. Polym Eng Sci 31(19):1411–1416. https://doi.org/10.1002/pen.760311907
46. Konaganti VK, Derakhshandeh M, Ebrahimi M, Mitsoulis E, Hatzikiriakos SG (2016) Non-isothermal extrudate swell. Phys Fluids 28(12):123101. https://doi.org/10.1063/1.4968826
47. Sierra J, Noriega Escobar M, Gómez JF, Pastor JM (2006) Isothermal and non-isothermal Crystallization Kinetics for Blends of Polyamide 6 and Polypropylene. Zeitschrift Kunststofftechnik/Journal of Plastics Technology
48. Kugele D, Dörr D, Wittemann F, Hangs B, Rausch J, Kärger L, Henning F (2017) Modeling of the non-isothermal crystallization kinetics of polyamide 6 composites during thermoforming. AIP Conference Proceedings 1896(1):030005 https://doi.org/10.1063/1.5007992 https://pubs.aip.org/aip/acp/article-pdf/doi/10.1063/1.5007992/14144197/030005_1_online.pdf
49. Schneider D, Schwab F, Schoof E, Reiter A, Herrmann C, Selzer M, Böhlke T, Nestler B (2017) On the stress calculation within phase-field approaches: a model for finite deformations. Comput Mech 60(2):203–217
50. Durga A, Wollants P, Moelans N (2013) Evaluation of interfacial excess contributions in different phase-field models for elastically inhomogeneous systems. Modell Simul Mater Sci Eng 21(5):055018
51. Mosler J, Shchyglo O, Montazer Hojjat H (2014) A novel homogenization method for phase field approaches based on partial rank-one relaxation. J Mech Phys Solids 68:251–266
52. Prahs A, Schöller L, Schwab FK, Schneider D, Böhlke T, Nestler B (2024) A multiphase-field approach to small strain crystal plasticity accounting for balance equations on singular surfaces. Comput Mech 73(4):773–794. https://doi.org/10.1007/s00466-023-02389-6
53. Shen F, Zhu W, Zhou K, Ke L-L (2021) Modeling the temperature, crystallization, and residual stress for selective laser sintering of polymeric powder. Acta Mech 232(9):3635–3653. https://doi.org/10.1007/s00707-021-03020-6
54. Cao Y, Ju Y, Liao F, Jin X, Dai X, Li J, Wang X (2016) Improving the flame retardancy and mechanical properties of poly(lactic acid) with a novel nanorod-shaped hybrid flame retardant. RSC Adv. 6:14852–14858. https://doi.org/10.1039/C5RA25112E
55. Kannenberg T, Schöller L, Prahs A, Schneider D, Nestler B (2024) Microstructure evolution accounting for crystal plasticity in the context of the multiphase-field method. Comput Mech. 74(1):67–84. https://doi.org/10.1007/s00466-023-02423-7
56. Schwab FK, Reiter A, Herrmann C, Schneider D, Nestler B (2020) Phase-inherent linear visco-elasticity model for infinitesimal deformations in the multiphase-field context. Adv Model Simul Eng Sci. https://doi.org/10.1186/s40323-020-00178-x
57. Voigt W (1889) Ueber die beziehung zwischen den beiden elasticitätsconstanten isotroper körper. Annalen der Physik. 274(12):573–587. https://doi.org/10.1002/andp.18892741206
58. Reuss A (1929) Berechnung der fließgrenze von mischkristallen auf grund der plastizitätsbedingung für einkristalle. Zeitschrift für

Angewandte Mathematik und Mechanik. 9(1):49–58. https://doi.org/10.1002/zamm.19290090104
59. Hill R (1963) Elastic properties of reinforced solids: some theoretical principles. J Mech Phys Solids. 11(5):357–372. https://doi.org/10.1016/0022-5096(63)90036-x
60. Reder M, Holland-Cunz J, Lorson P, August A, Nestler B Simulative determination of effective mechanical properties for digitally generated foam geometries. Adv Eng Mater. (2023) https://doi.org/10.1002/adem.202300340
61. Hashin Z, Shtrikman S (1963) A variational approach to the theory of the elastic behaviour of multiphase materials. J Mech Physics Solids. **11**(2), 127–140 https://doi.org/10.1016/0022-5096(63)90060-7
62. Nguyen S-T, Thai M-Q, Vu M-N, To Q-D (2016) A homogenization approach for effective viscoelastic properties of porous media. Mech Mater. 100:175–185. https://doi.org/10.1016/j.mechmat.2016.06.015
63. Barral M, Chatzigeorgiou G, Meraghni F, Léon R (2020) Homogenization using modified mori-tanaka and tfa framework for elastoplastic-viscoelastic-viscoplastic composites: Theory and numerical validation. Int J Plast. 127:102632. https://doi.org/10.1016/j.ijplas.2019.11.011
64. Guo R, Ren Z, Bi H, Xu M, Cai L (2019) Electrical and thermal conductivity of polylactic acid (pla)-based biocomposites by incorporation of nano-graphite fabricated with fused deposition modeling. Polymers 11(3):549
65. Graczykowski B, El Sachat A, Reparaz JS, Sledzinska M, Wagner MR, Chavez-Angel E, Wu Y, Volz S, Wu Y, Alzina F, Sotomayor Torres CM (2017) Thermal conductivity and air-mediated losses in periodic porous silicon membranes at high temperatures. Nat. Commun. 8(1):415
66. Wang Y, Wang P (2020) Analysis on the determination of specific heat of air at constant pressure. IOP Conf. Ser. Earth Environ. Sci. 474(5):052021
67. Orellana Barrasa J, Ferrández-Montero A, Ferrari B, Pastor JY (2021) Characterisation and modelling of PLA filaments and evolution with time. Polymers (Basel) 13(17):2899
68. Jones FE (1978) The air density equation and the transfer of the mass unit. J. Res. Natl. Bur. Stand. 83(5):419–428
69. Benson T Air Properties Definitions — grc.nasa.gov. https://www.grc.nasa.gov/www/k-12/BGP/airprop.html. [Accessed 07-05-2024]
70. Yousefzade O, Jeddi J, Vazirinasab E, Garmabi H (2018) Poly(lactic acid) phase transitions in the presence of nano calcium carbonate: opposing effect of nanofiller on static and dynamic measurements. J Thermoplast Compos Mater. 32:089270571875938. https://doi.org/10.1177/0892705718759386
71. Ansys Granta Edupack: Polylactide (PLA). In *PLA Datasheet*, pp. 1-5
72. SA S Shrinkage Value of Plastics Material & Injection Molding - Chart — omnexus.specialchem.com. https://omnexus.specialchem.com/polymer-property/shrinkage. [Accessed 07-05-2024]
73. Pivar M, Gregor-Svetec D, Muck D (2022) Effect of printing process parameters on the shape transformation capability of 3d printed structures. Polymers. https://doi.org/10.3390/polym14010117
74. Wang X, Zhao L, Fuh JYH (2019) Lee HP Effect of porosity on mechanical properties of 3d printed polymers: experiments and micromechanical modeling based on x-ray computed tomography analysis. Polymers. https://doi.org/10.3390/polym11071154
75. Liao Y, Liu C, Coppola B, Barra G, Di Maio L, Incarnato L, Lafdi K (2019) Effect of porosity and crystallinity on 3d printed pla properties. Polymers. https://doi.org/10.3390/polym11091487
76. Heuer A, Huether J, Liebig WV, Elsner P (2021) Fused filament fabrication: comparison of methods for determining the interfacial strength of single welded tracks. Manuf Rev. 8:32. https://doi.org/10.1051/mfreview/2021031
77. McIlroy C, Graham RS (2018) Modelling flow-enhanced crystallisation during fused filament fabrication of semi-crystalline polymer melts. Addit Manuf 24:323–340. https://doi.org/10.1016/j.addma.2018.10.018
78. Northcutt LA, Orski SV, Migler KB, Kotula AP (2018) Effect of processing conditions on crystallization kinetics during materials extrusion additive manufacturing. Polymer. 154:182–187. https://doi.org/10.1016/j.polymer.2018.09.018
79. Djellali S, Sadoun T, Haddaoui N, Bergeret A (2015) Viscosity and viscoelasticity measurements of low density polyethylene/poly(lactic acid) blends. Polymer. 72(5):1177–1195. https://doi.org/10.1007/s00289-015-1331-6
80. Duhduh AA, Noor HH, Kundu A, Coulter JP Advanced Additive Manufacturing of Functionally Gradient Multi Material Polymer Components with Single Extrusion Head: Melt Rheology Analysis. In: ANTEC 2019
81. Wang H, Rabhi F, Cherouat A, Gilbin A, Barriere T (2023) Experimental and numerical investigation of extrudate swell of polylactic acid via extrusion-based additive manufacturing process. Int. J. Adv. Manuf, Technol
82. Yoo HM, Jeong S-Y, Choi S-W (2021) Analysis of the rheological property and crystallization behavior of polylactic acid (ingeo™ biopolymer 4032d) at different process temperatures. e-Polymers 21(1):702–709. https://doi.org/10.1515/epoly-2021-0071